



NIRS-SPM: Statistical parametric mapping for near-infrared spectroscopy

Jong Chul Ye ^{*}, Sungho Tak ¹, Kwang Eun Jang, Jinwook Jung, Jaeduck Jang

Bio Imaging and Signal Processing Laboratory, Department of Bio and Brain Engineering, Korea Advanced Institute of Science and Technology (KAIST), 373-1 Guseong-dong Yuseong-gu, Daejon 305-701, Korea

ARTICLE INFO

Article history:

Received 8 January 2008

Revised 21 August 2008

Accepted 26 August 2008

Available online 12 September 2008

Keywords:

Near infrared spectroscopy

General linear model

Excursion statistics

Inhomogeneous Gaussian random field

Tube formula

Incomplete gamma bound

ABSTRACT

Near infrared spectroscopy (NIRS) is a non-invasive method to measure brain activity via changes in the degree of hemoglobin oxygenation through the intact skull. As optically measured hemoglobin signals strongly correlate with fMRI BOLD signals, simultaneous measurement using NIRS and fMRI promises a significant mutual enhancement of temporal and spatial resolutions. Although there exists a powerful statistical parametric mapping tool in fMRI, current public domain statistical tools for NIRS have several limitations related to the quantitative analysis of simultaneous recording studies with fMRI. In this paper, a new public domain statistical toolbox known as NIRS-SPM is described. It enables the quantitative analysis of NIRS signal. More specifically, NIRS data are statistically analyzed based on the general linear model (GLM) and Sun's tube formula. The *p*-values are calculated as the excursion probability of an *inhomogeneous* random field on a representation manifold that is dependent on the structure of the error covariance matrix and the interpolating kernels. NIRS-SPM not only enables the calculation of activation maps of oxy-, deoxy-hemoglobin and total hemoglobin, but also allows for the super-resolution localization, which is not possible using conventional analysis tools. Extensive experimental results using finger tapping and memory tasks confirm the viability of the proposed method.

© 2008 Elsevier Inc. All rights reserved.

Introduction

Near-infrared spectroscopy (NIRS) is a non-invasive method to monitor brain activity by measuring the absorption of the near-infrared light between 650 nm and 950 nm through the intact skull (Villringer and Dirnagl, 1995). Specifically, the absorption spectra of oxy-hemoglobin (HbO) and deoxy-hemoglobin (HbR) are distinct in this region; thus, it is possible to determine concentration changes of oxy- and deoxy-hemoglobin from diffusely scattered light measurements (Jobsis, 1977). NIRS has many advantages over other neuroimaging modalities such as positron emission tomography (PET), functional magnetic resonance imaging (fMRI) or magnetoencephalography (MEG). One of its main advantages is the ability to directly measure a wide range of functional contrasts such as oxy-hemoglobin, deoxy-hemoglobin, and total hemoglobin directly with very high temporal resolution. This enables the study of the temporal behaviors of the hemodynamic response to neural activation. In contrast, the fMRI BOLD signal is physiologically ambiguous due to the coupling of the cerebral blood flow (CBF), oxidative metabolism, and the cerebral blood volume (CBV) (Logothetis, 2003; Hoge et al., 2005). Another advantage of NIRS is the high degree of flexibility in its experimental use, as NIRS requires only a compact measurement system and is robust to the motion artifact compared to fMRI. However, NIRS lacks

anatomical information, making it difficult to localize the brain area from which the NIRS signal originates (Homan et al., 1987; Okamoto et al., 2004a). Moreover, NIRS has poor spatial resolution and limited penetration depth due to the high level of light scattering within the tissue.

Simultaneous recording with NIRS and fMRI can provide a solution to overcome these disadvantages. Over the past ten years, several groups have conducted extensive researches in this area (Kleinschmidt et al., 1996; Benaron et al., 2000; Hess et al., 2000; Toronov et al., 2001; Cannestra et al., 2001; Murata et al., 2002; Strangman et al., 2002; Yamamoto and Kato, 2002; Mehagnoul-Schipper et al., 2002; Toronov et al., 2003; Boas et al., 2003; Chen et al., 2003; MacIntosh et al., 2003; Siegel et al., 2003; Mandeville et al., 1999; Okamoto et al., 2004b; Fujiwara et al., 2004). An excellent review of these methods is available in Steinbrink et al. (2006). Most of these studies found that an optically measured hemoglobin signal strongly correlates with the fMRI BOLD signal, although the exact oxygen species with the best correlation remains controversial.² Furthermore, the integration of NIRS with fMRI can reveal not only the hemodynamic aspects of brain activation but also metabolic variables such as the oxygen extraction fraction (OEF) and the cerebral metabolic rate for oxygen consumption (CMRO_2) (Hoge et al., 2005).

* Corresponding author.

E-mail address: jong.ye@kaist.ac.kr (J.C. Ye).

¹ Co-first author with equal contribution.

² Currently, it is generally agreed that the oxy-hemoglobin signal has a higher signal-to-noise ratio, whereas the deoxy-hemoglobin signal is more specific to the activation area and follows the BOLD signal more closely (Huppert et al., 2006).

However, several technical challenges remain for quantitative analyses of simultaneous NIRS and fMRI recordings. First, the differential path length factor (DPF) in the modified Beer-Lambert law (MBLL) (Cope and Delpy, 1988) is highly variable depending on the subject or the measurement system (Zhao et al., 2002). It is well-known that an incorrect DPF not only results in quantitatively incorrect estimates of the oxy- and deoxy-hemoglobin concentrations, but also introduces crosstalk between the two measurements (Hoshi, 2007). Although a DPF parameter can be measured using time domain or frequency domain systems by calculating the temporal point spread function (Zhao et al., 2002), this information is not obtainable in commonly available continuous wave (CW) systems. As an alternative, the diffuse optical tomography (DOT) technique has been investigated. In this technique, the DPF is not necessary due to the nature of the tomographic reconstruction from multi-channel measurements (Boas et al., 2001). While several promising DOT reconstruction techniques have been demonstrated for brain imaging (Boas et al., 2004), most often require *a priori* knowledge of the optical parameters for the detailed anatomical structure of brain, and the imaging problem is a significant problem due to the limited amount of light penetration. Therefore, further investigations must be conducted before wide acceptance of DOT for brain mapping occurs.

Moreover, unlike PET and fMRI, no standard methods of NIRS data analyses are currently available, and different groups have performed an analysis based on different sophisticated analysis tools. The classical approach is a paired *t*-test that examines whether or not the signal changes due to activation are statistically significant. One of the most popular tools in this regard is a custom Matlab program known as HomER (available at <http://www.nmr.mgh.harvard.edu/PMI/>). In HomER, no fixed canonic hemodynamic response is assumed in order to avoid any systemic errors from an incorrect model. Rather, the individual hemodynamic response is calculated using ordinary least-squared linear deconvolution. However, these approaches also rely on time-line analysis approaches (Obreg and Villringer, 2003) for which specific differential path length factors (DPF) should be assumed.

Currently, many research groups are developing statistical analysis toolboxes for NIRS that are based on the generalized linear model (GLM) (Schroeter et al., 2004; Plichta et al., 2007; Koh et al., 2007). GLM is a statistical linear model that explains data as a linear combination of an explanatory variable plus an error term. As GLM measures the temporal variational pattern of signals rather than their absolute magnitude, GLM is robust in many cases, even in cases with incorrect DPF and severe optical signal attenuation due to scattering or poor contact. In an event-related paradigm, Plichta et al. (2007) showed that the GLM-based approach provides a statistically more powerful test of the activation compared to the conventional approaches. Furthermore, as GLM has become the standard method for analyzing the fMRI data (Worsley and Friston, 1995), an integration of NIRS and fMRI within the same GLM framework may have an advantage when modeling both types of data in the same mathematical framework to make an inference. For example, Koh et al. (2007) developed extensive statistical NIRS analysis tools termed functional optical signal analysis (fOSA). This tool applies the SPM method to NIRS data.

However, several fundamental issues remain to be addressed. For example, a measure of concern regarding the GLM approach exists, as the canonical hemodynamic response or box car functions are used as predictors for both HbR and HbO without accounting for both their differences and the dependency on individual subjects (Hoshi, 2007). Furthermore, the basic assumption of the Gaussian random field model in fOSA breaks down in NIRS. It is important to note that SPM for an fMRI analysis assumes that the residuals after the GLM fitting are dense samples on lattice representations from an underlying homogeneous Gaussian random field due to Gaussian kernel smoothing (Friston et al., 1996). However, as the distance between each channel of NIRS is great and because the number of measurements is small, it is not feasible to use homogeneous Gaussian random field

theory when making inferences of NIRS data. Finally, the resolution of fOSA is limited by the distance between the optodes, which makes it difficult to co-registered with the fMRI activation map. In order to address the co-registration problem, Schroeter et al. (2004) applied spectral analysis methods to calculate a map of the power spectral density, coherence and phase. Here, pixels with less than 50% coherence to the most activated pixel were declared non-active, and the phase values were calculated for only the active pixels. Other type of exact channel-wise statistics have been also used in literature (Plichta et al., 2006, 2007; Okamoto et al., 2006; Hofmann et al., 2008). However, we are not aware of any approach that addresses the exact excursion probability for the interpolated random fields in between channels.

The main contribution of the present article is the presentation of new statistical parameter mapping for NIRS. The corresponding software known as NIRS-SPM is publicly available at the website of the authors (<http://bisb.kaist.ac.kr/NIRS-SPM>). NIRS signal analysis requires the excursion probability of the *inhomogeneous* Gaussian random field that is generated by the *interpolated* samples from *sparingly* and *irregularly* distributed optode measurements. The situation is drastically different from a SPM analysis for EEG/MEG, in which a three-dimensional dense map of source distribution is initially obtained by solving an inverse problem. Rather than resorting to a full 3-D reconstruction using DOT, this study focuses on a topographic 2-D reconstruction of the cortical cortex. Interestingly, the resultant reconstruction is an interpolation from the results of each channel SPM using inhomogeneous interpolation kernels. The resultant random field from such an interpolation is an inhomogeneous Gaussian random field, similar to those encountered voxel based morphometry (VBM) studies. Non-stationary random field theory is used to find accurate *p*-values for local maxima. For example, Taylor and Worsley (2007, 2008) showed that the Gaussian random field theory can be accurately extended to non-isotropic cases by replacing the intrinsic volume expression in Euler characteristics with Lipschitz-Killing curvature that incorporates the information from the local correlation function of the underlying inhomogeneous Gaussian random fields. Similar results have been reported elsewhere (Worsley et al., 1999). We have also found that 3-D parametric shape estimation problem in a computer vision problem (Ye et al., 2006) has also a striking similarity to the current problem setup. Ye et al. (2006) use Sun's tube formula (Sun, 1993; Cao and Worsley, 1999a) for calculating the excursion probability of an inhomogeneous Gaussian random field that originates from interpolated parametric surface estimates from sparse noisy measurements. In the Gaussian SPMs, Sun's tube formula and random field theory give the same solution (Takemura and Kuriki, 2002). Due to these powerful tools for calculating the excursion probability, NIRS-SPM not only enables a calculation of activation maps for HbO, HbR and HbT, but also allows super-resolution localization, which was not possible when using other conventional methods.

This paper also describes several additional techniques for optimizing NIRS-SPM. First, in an estimation of the temporal correlations, the precoloring (Worsley and Friston, 1995) and prewhitening methods (Bullmore et al., 1996; Friston et al., 2002) originally introduced in the fMRI model are compared. Although the prewhitening method adapted from fMRI-SPM (Friston et al., 2006) is, in theory, statistically the most efficient approach and has been employed in most of the NIRS-GLM analyses for temporal correlation correction (Plichta et al., 2006, 2007; Koh et al., 2007; Hofmann et al., 2008), the difference between the assume and the actual correlations due to the small number of channels in NIRS can produce bias that has effects on the inference. Hence, an appropriate method of estimating the temporal correlations in NIRS data is proposed. Second, distinct predictor models for oxy- and deoxy-hemoglobin are derived and analyzed. Finally, in order to localize the NIRS signal to the cerebral cortex of an anatomical T1 image obtained from MRI, Horn's algorithm (Horn, 1987) is implemented in NIRS-SPM. Finding the relationship between

the actual 3-D space and the MR image domain using pairs of coordinates in both systems is a well-known problem known as absolute orientation. A closed-form, least-square solution for this problem is implemented as described in Horn (1987).

This paper is organized as follows. In Theory section, the theory of NIRS-SPM is discussed in detail. Method section provides additional implementation issues of NIRS-SPM, which is followed by the experimental results regarding finger tapping and working memory tasks in Experimental results section. Discussion section discusses the limitation of the NIRS-SPM. Conclusions are presented in Conclusion section.

Theory

Measurement model for NIRS

According to the modified Beer–Lambert law (MBLL) (Cope and Delpy, 1988), the optical density variation $\Delta\phi(r, s; \lambda, t)$ (unitless quantity) at time t due to HbO and HbR concentration changes (Δc_{HbO} , Δc_{HbR}) [μM] is described as

$$\begin{aligned}\Delta\phi(r, s; \lambda, t) &= -\ln \frac{U(r, s; \lambda, t)}{U_0(r, s; \lambda)} \\ &= [a_{\text{HbO}}(\lambda)\Delta c_{\text{HbO}}(r, t) + a_{\text{HbR}}(\lambda)\Delta c_{\text{HbR}}(r, t)]d(r)l(r)\end{aligned}\quad (1)$$

where (r, s) denotes the detector and source position, λ is the wavelength of the laser source, $U(r, s; \lambda, t)$ denotes the measured photon flux at time t , $U_0(r, s; \lambda)$ denotes the initial photon flux, $a_{\text{HbO}}(\lambda)$ [$\mu\text{M}^{-1} \text{mm}^{-1}$] and $a_{\text{HbR}}(\lambda)$ [$\mu\text{M}^{-1} \text{mm}^{-1}$] are the extinction coefficients of the HbO and HbR, $d(r)$ is the unitless differential path length factor (DPF), and $l(r)$ [mm] is the distance between the source and the detector at the position r , respectively.

The MBLL indicates that HbO and HbR concentration changes can be estimated using the optical density measurements at two wavelengths. More specifically, let $\{(r_i, s_i)\}_{i=1}^K$ denotes the set of detector and source pairs in this case. Initially defined is

$$\begin{bmatrix} \Delta\phi_{\text{HbO}}(r_i, s_i; t) \\ \Delta\phi_{\text{HbR}}(r_i, s_i; t) \end{bmatrix} = \begin{bmatrix} a_{\text{HbO}}(\lambda_1) & a_{\text{HbR}}(\lambda_1) \\ a_{\text{HbO}}(\lambda_2) & a_{\text{HbR}}(\lambda_2) \end{bmatrix}^{-1} \begin{bmatrix} \Delta\phi(r_i, s_i; \lambda_1, t) \\ \Delta\phi(r_i, s_i; \lambda_2, t) \end{bmatrix}. \quad (2)$$

The HbX (i.e., HbO or HbR) concentration changes are then obtained by

$$\Delta c_{\text{HbX}}(r_i, s_i; t) = \frac{\Delta\phi_{\text{HbX}}(r_i, s_i; t)}{d(r)l(r)}. \quad (3)$$

Here, ambiguities exist that are related to the calculated HbX variation in Eq. (3), as the distances between the source and detector are relatively large and the hemoglobin concentration changes could locate at any point between source and detectors. Moreover, there exists only a small number of optodes that are distributed irregularly, which makes the NIRS imaging of the brain very difficult.

Although Eq. (1) is used extensively, this is merely a first-order approximation of diffusive light scattering. More specifically, in a highly scattering media such as the brain, the photon path from CW illumination can be described using the following diffusion equation (Boas et al., 1997):

$$D_0 \nabla^2 U_0(r, s; \lambda) - \mu_a^0(r; \lambda) U_0(r, s; \lambda) = -\delta(r-s). \quad (4)$$

Here, $U_0(r, s; \lambda)$ denotes the photon flux at r when the laser source of wavelength λ with unit intensity is located at s , $\mu_a^0(r; \lambda)$ denotes the absorption coefficient at the rest stage, and D_0 represents the homogenous diffusion coefficients. Here, the HbO and HbR concentration changes the results of the absorption coefficient.

$$\Delta\mu_a(r; \lambda, t) = a_{\text{HbO}}(\lambda)\Delta c_{\text{HbO}}(r, t) + a_{\text{HbR}}(\lambda)\Delta c_{\text{HbR}}(r, t) \quad (5)$$

Under the first order Rytov approximation, the optical density change can then be approximated as follows (O'Leary et al., 1995):

$$\Delta\phi(r, s; \lambda, t) = -\ln \frac{U(r, s; \lambda, t)}{U_0(r, s; \lambda)} \approx \int dr' \frac{U_0(r, r'; \lambda)U_0(r', s; \lambda)}{U_0(r, s; \lambda)} \Delta\mu_a(r'; \lambda, t). \quad (6)$$

Here, $U_0(r, r'; \lambda)$ denotes the homogenous Green's function from Eq. (10) by putting the source at r' . In a comparison of Eq. (1) with Eq. (12), the MBLL is shown to be an approximation of Eq. (12) when the absorption change is local, i.e. $\Delta\mu_a(r'; \lambda, t) = \Delta\mu_a(r'; t)\delta(r-r')$.

Interestingly, the Rytov approximation in Eq. (6) provides a solution that addresses the drawbacks of the MBLL-based conventional approaches. More specifically, in a case in which $\{(r_i, s_i)\}_{i=1}^K$ denotes the detector and source pairs, Appendix A shows that the estimate of HbX (i.e. HbO or HbR) changes at any position r can be interpolated using the $\{\Delta\phi_{\text{HbX}}(r_i, s_i; t)\}_{i=1}^K$:

$$\Delta c_{\text{HbX}}(r, t) = \sum_{i=1}^K B_i(r) \Delta\phi_{\text{HbX}}(r_i, s_i; t) \quad (7)$$

where $B_i(\cdot)$ corresponds to the inhomogeneous interpolation kernel derived from the diffusion equation and spatial correlation with adjacent channel hemoglobin status. Due to the interpolation relationship in Eq. (7), the statistical testing of $\Delta c_{\text{HbX}}(r, t)$ can be directly transferred from the statistical testing of $\Delta\phi_{\text{HbX}}(r_i, s_i, t)$. This will be discussed in the sequel.

General linear model

This section focuses on the GLM of $\Delta\phi_{\text{HbX}}(r_i, s_i; t)$. The GLM can be easily transferred to the interpolated measurement $\Delta c_{\text{HbX}}(r, t)$ due to the interpolation relationship of Eq. (7).

Here, $y^{(i)} \in \mathbb{R}^N$ and $\epsilon^{(i)} \in \mathbb{R}^N$ are temporal samples given by

$$y^{(i)} = [\Delta\phi_{\text{HbX}}(r_i, s_i; t_1) \ \Delta\phi_{\text{HbX}}(r_i, s_i; t_2) \cdots \Delta\phi_{\text{HbX}}(r_i, s_i; t_N)]^T, \quad (8)$$

$$\epsilon^{(i)} = [\epsilon(r_i, s_i; t_1) \ \epsilon(r_i, s_i; t_2) \cdots \epsilon(r_i, s_i; t_N)]^T, \quad (9)$$

where $\epsilon(r_i, s_i; t)$ denotes the zero-mean Gaussian noise at time t . The corresponding GLM model is then given by

$$y = (I_K \otimes X)\beta + \epsilon \quad (11)$$

where $X \in \mathbb{R}^{N \times M}$ denotes the design matrices, and $\beta^{(i)} \in \mathbb{R}^M$ is the corresponding response signal strength at the i -th channel. Stacking the measurements from all K channels gives

$$y = \begin{bmatrix} y^{(1)} \\ y^{(2)} \\ \vdots \\ y^{(K)} \end{bmatrix}, \quad \beta = \begin{bmatrix} \beta^{(1)} \\ \beta^{(2)} \\ \vdots \\ \beta^{(K)} \end{bmatrix}, \quad \epsilon = \begin{bmatrix} \epsilon^{(1)} \\ \epsilon^{(2)} \\ \vdots \\ \epsilon^{(K)} \end{bmatrix}. \quad (12)$$

As described in Appendix B, the noise covariance matrix from the SPM assumption is given by

$$C_\epsilon = E[\epsilon\epsilon^T] = \begin{bmatrix} \sigma^{(1)^2} \Lambda & \mathbf{0} & \cdots & \mathbf{0} \\ \mathbf{0} & \sigma^{(2)^2} \Lambda & \cdots & \mathbf{0} \\ \vdots & \vdots & \ddots & \vdots \\ \mathbf{0} & \mathbf{0} & \cdots & \sigma^{(K)^2} \Lambda \end{bmatrix} = \Sigma \otimes \Lambda \quad (13)$$

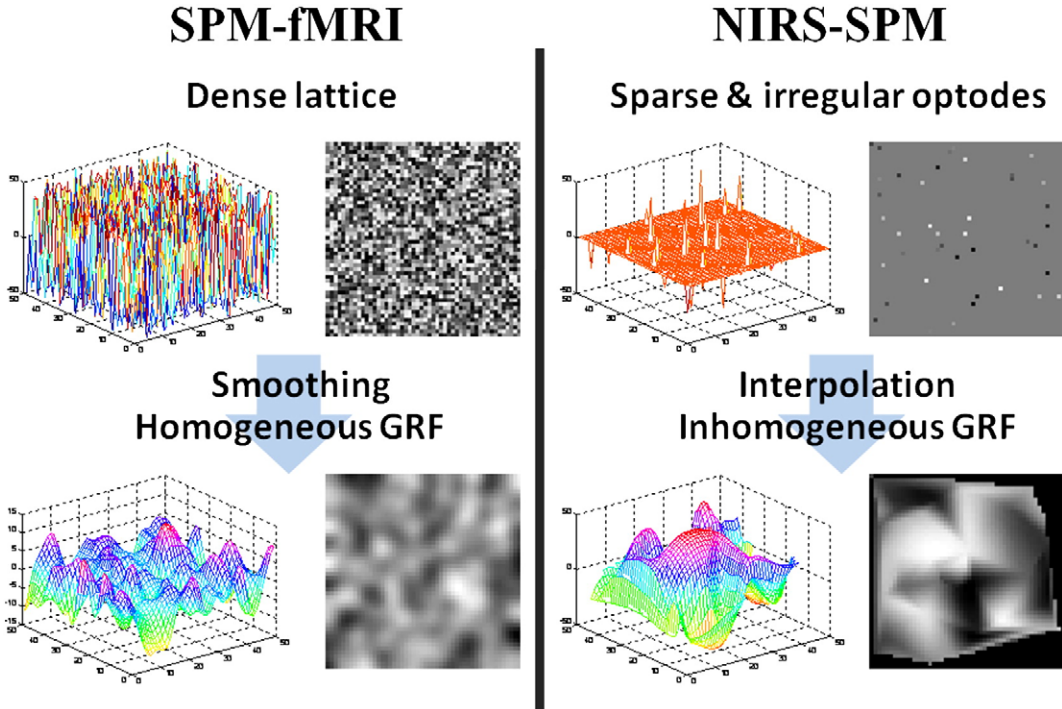


Fig. 1. Comparison between the conventional SPM and NIRS-SPM. The Gaussian random field (GRF) assumption in fMRI analysis is based on the Gaussian kernel smoothing on a dense lattice. However, the situation is drastically different in NIRS since only a sparse number of optodes are located irregularly. NIRS-SPM first interpolates the data using inhomogeneous Gaussian random field theory.

where Λ denotes the common temporal correlation matrix for all channels and

$$\Sigma = \begin{bmatrix} \sigma^{(1)^2} & \mathbf{O} & \cdots & \mathbf{O} \\ \mathbf{O} & \sigma^{(2)^2} & \cdots & \mathbf{O} \\ \vdots & \vdots & \ddots & \vdots \\ \mathbf{O} & \mathbf{O} & \cdots & \sigma^{(K)^2} \end{bmatrix} \quad (14)$$

Then, the least-square estimation of β and its error covariance matrix are given by

$$\hat{\beta} = (\mathbf{I}_K \otimes \mathbf{X}^\dagger) \mathbf{y}, \quad \mathbf{C}_{\hat{\beta}} = \Sigma \otimes (\mathbf{X}^\dagger \Lambda \mathbf{X}^{\dagger T}), \quad (15)$$

where \mathbf{X}^\dagger denotes the pseudo-inverse of \mathbf{X} . The response signal strength $\alpha(r)$ at the any location r then can be estimated from β as described in Appendix C:

$$\alpha(r) = (\mathbf{b}(r)^T \otimes \mathbf{I}_M) \hat{\beta} \in \mathbb{R}^M. \quad (16)$$

Here, the basis vector $\mathbf{b}(r)$ is given by stacking $B_i(r)$ into a vector:

$$\mathbf{b}(r) = [B_1(r) \quad B_2(r) \quad \cdots \quad B_K(r)]^T \in \mathbb{R}^K. \quad (17)$$

Furthermore, its error covariance is given by

$$\mathbf{C}_\alpha = (\mathbf{b}(r)^T \Sigma \mathbf{b}(r)) \otimes (\mathbf{X}^\dagger \Lambda \mathbf{X}^{\dagger T}) \in \mathbb{R}^{M \times M}. \quad (18)$$

Inference

Usually, the response of the signal of interest here is calculated by an inner product with a contrast vector $\mathbf{c} \in \mathbb{R}^M$

$$\hat{\chi}(r) = \mathbf{c}^T \hat{\alpha}(r) \quad (19)$$

Using Eq. (18), the corresponding error variance is

$$C_{\hat{\chi}}(r) = (\mathbf{b}(r)^T \Sigma \mathbf{b}(r)) (\mathbf{c}^T \mathbf{X}^\dagger \Lambda \mathbf{X}^{\dagger T} \mathbf{c}) \quad (20)$$

Under the null hypothesis the response signal $\hat{\chi}(r)$ is distributed as a zero-mean Gaussian distribution:

$$\hat{\chi}(r) \sim N(0, C_{\hat{\chi}}(r)) \quad (21)$$

Hence, the corresponding t -statistics is given by

$$T(r) = \frac{\mathbf{c}^T \hat{\alpha}(r)}{\sqrt{(\mathbf{b}(r)^T \Sigma \mathbf{b}(r)) (\mathbf{c}^T \mathbf{X}^\dagger \Lambda \mathbf{X}^{\dagger T} \mathbf{c})}} \quad (22)$$

where the effective degrees of freedom is given by:

$$df = \frac{\text{trace}(\mathbf{R}\Lambda)^2}{\text{trace}(\mathbf{R}\Lambda\mathbf{R}\Lambda)}. \quad (23)$$

with the residual forming matrix $\mathbf{R} = \mathbf{I} - \mathbf{X}(\mathbf{X}^T \mathbf{X})^{-1} \mathbf{X}^T$ (Worsley and Friston, 1995).

At this point, the goal is to calculate the p -value for which the null hypothesis can be abandoned. This can be calculated as an excursion probability of the resultant random field. More specifically, the interest here is in calculating the following excursion probabilities:

One side t -test: $P[\max_{r \in \Psi} T(r) \geq z]$.

While the form of the excursion probability appears similar to that of the excursion probability of a Gaussian random field in SPM for fMRI, fundamental differences exist. As illustrated in Fig. 1, the Gaussian random field in fMRI comes from the Gaussian kernel smoothing of discrete signals on a dense lattice, whereas the proposed excursion probability comes from the random field that is interpolated from sparsely and irregularly distributed measurements. The interpolation step from irregularly distributed samples through diffusive medium causes the resultant random field to become inhomogeneous; hence, it is not possible to use a p -value that is tailored to the homogeneous Gaussian random field. The situation is slightly different in EEG/MEG, where all of the channel measurements can be used for interpolating the measurement at r , as electro-magnetic signals can be transmitted through the brain. In this case, it can be expected that the resultant

random field is homogeneous. However, in NIRS, the signal is highly attenuated, and the interpolation steps of Eq. (13) only use the information from adjacent channels. Hence, the resultant random field is inhomogeneous.

We then use random field theory results, which are in fact available for practically any non-homogeneous random field, even on manifolds, provided that it is smooth (Worsley et al., 1999; Taylor and Adler, 2003; Taylor and Worsley, 2008; Ye et al., 2006). Among these methods, we follow Ye et al. (2006) and employ Sun's tube formula (Sun, 1993; Cao and Worsley, 1999b) to calculate the excursion statistics of the resultant inhomogeneous random field since the formulation is strikingly similar. More specifically, the resultant p -value can be calculated as described in Appendix D:

$$p = P\left\{\max_{r \in \Psi} T(r) \geq z\right\} \approx \frac{\kappa_0}{\omega_D} \left(1 - \Gamma\left(\frac{D+1}{2}, \frac{z^2}{2}\right)\right) \quad (24)$$

where $\omega_D = 2\pi^{(D+1)/2}/\Gamma\left(\frac{D+1}{2}\right)$ denotes the surface area of the $(D+1)$ -dimensional unit sphere, and κ_0 is given by

$$\kappa_0 = \int_{\Psi} \sqrt{|\det(\nabla u(r) \nabla^T u)|} dr \quad (25)$$

for the unit vector $u \in \mathbb{R}^K$:

$$u = \frac{C_{\hat{\beta}}^{1/2} (b(r)^T \otimes I_M) c}{\sqrt{b(r)^T \Sigma b(r)} \sqrt{c^T X^{\dagger} A X^{\dagger} c}} \quad (26)$$

Method

Behavior protocol

To evaluate the practicality of the proposed methods, NIRS-SPM was applied to a right finger tapping (RFT) exercise and to working memory experimental data. For the RFT tasks, the block paradigm and the event-related paradigm were used. For the working memory experiment, only the block paradigm was used. As the target area of the finger tapping task and the working memory experiments were within the primary motor cortex and prefrontal/Broca's area, respectively, these tasks are within the limit of the penetration depth of NIRS; hence, they are used fairly often in NIRS experiments (Kleinschmidt et al., 1996; Toronov et al., 2001; Murata et al., 2002; Strangman et al., 2002; Yamamoto and Kato, 2002; Mehagnoul-Schipper et al., 2002; Toronov et al., 2003; Boas et al., 2003; Tsujimoto et al., 2004; Hoshi et al., 2003).

In the case of block design finger tapping, a 21-second period of activation alternated with a 30-second period of rest. This was repeated 10 times for each subject. The total recording time was 552 s. For the event-related finger tapping task, the task periods were 2 s and the interstimulus interval was pseudo-randomly chosen with an average of 12 s (ranging from 4 to 20 s) (Huppert et al., 2006). The total recording time was 650 s. During the task period, subjects were instructed to perform a finger flexion and extension action repeatedly.

Table 1

NIRS and fMRI results of three excluded subjects in block-designed finger tapping task

	Subject 1	Subject 2	Subject 3
Oxy-hemoglobin	×	×	△
Deoxy-hemoglobin	×	×	×
Totalhemoglobin	×	×	△
fMRI	×	○	○

○: Activation in the target region. △: Activation in non-target region. ×: No significant activation ($p < 0.05$, NIRS: tube formula correction, fMRI: random field correction).

Table 2

NIRS and fMRI results of three excluded subjects in block-designed working memory task

	Subject 1	Subject 2	Subject 3
Oxy-hemoglobin	×	△	×
Deoxy-hemoglobin	×	×	×
Total-hemoglobin	×	△	×
fMRI	○	○	○

○: Activation in the target region. △: Activation in non-target region. ×: No significant activation ($p < 0.05$, NIRS: tube formula correction, fMRI: uncorrected).

In order to avoid eye and head movements, subjects were instructed to focus on a fixed point in the rest condition.

The paradigm of the working memory task was designed based on Wei et al. (2004), Smith et al. (1998). The experiment consisted of 16 task blocks (8 blocks for 2-back, 8 blocks for 0-back) and 16 rest blocks. Each block was 30 s. The total recording time was 522 s. During task period, a random series of single-digit numbers (1–9) was presented at the rate of one number every 2 s. During the 2-back task, subjects were instructed to press a key when each digit was identical to the one presented two digits previously in the series.

Subject selection

For block design finger tapping task, a total of 12 subjects were examined (mean age = 26.4 ± 2.5 years). Three subjects were excluded; one subject had no activated region from NIRS and fMRI, another had no activation in NIRS but has activation in fMRI, and the other subject had no activation in HbR, non-ROI activation in HbO and HbT, and activation in fMRI (See Table 1). All of the remaining 9 subjects were included for further analysis. For the event-related RFT task, a total of 9 subjects were examined (mean age = 23 ± 2.2 years). For the block design working memory task, a total of 11 subjects were examined (mean age = 25.8 ± 2.5 years). Three subjects were excluded (See Table 2). All of the remaining 8 subjects were included for further analysis.

All subjects were strongly right-handed. No subjects had a history of any neurological disorder. After all of the subjects were given instruction concerning the experimental environment and the operating mode of NIRS and MRI, signed informed consent forms were obtained. This study was approved by the Institutional Review Board of the Korea Advanced Institute of Science and Technology (KAIST).

Data acquisition

A continuous wave NIRS instrument (Oxymon MK III, Artinis, Netherlands) was used to measure changes in the optical density. The sampling rate was approximately 10 Hz. The NIRS system emits 781 nm and 856 nm laser lights at each source fiber. The NIRS system has 24 channels with eight sources and four detectors, as shown in Fig. 2, and it measures optical density variation in Eq. (1) for each channel. A holder cap to fix the distance between the source and detector optodes was attached to the scalp around the left primary motor cortex, dorsolateral prefrontal cortex, and Broca's area. The distance between the source and the detector was 3.5 cm. The fiber length was 10 m to connect the optodes in the MR scanner to the NIRS instrument in the MR control room.

A 3.0 T MRI system (ISOL, Republic of Korea) was used to measure the BOLD response. During the blocked task paradigm, the echo planar imaging (EPI) sequence was used with TR/TE = 3000/35 ms, flip angle = 80°, 35 slices, 4 mm slice thickness. In the event-related task paradigm, the EPI sequence was used as well (with TR/TE = 2000/35 ms, flip angle = 80°, 24 slices, 4 mm slice thickness). In the subsequent anatomical scanning session, T1-weighted structural images were acquired using the same scanner.

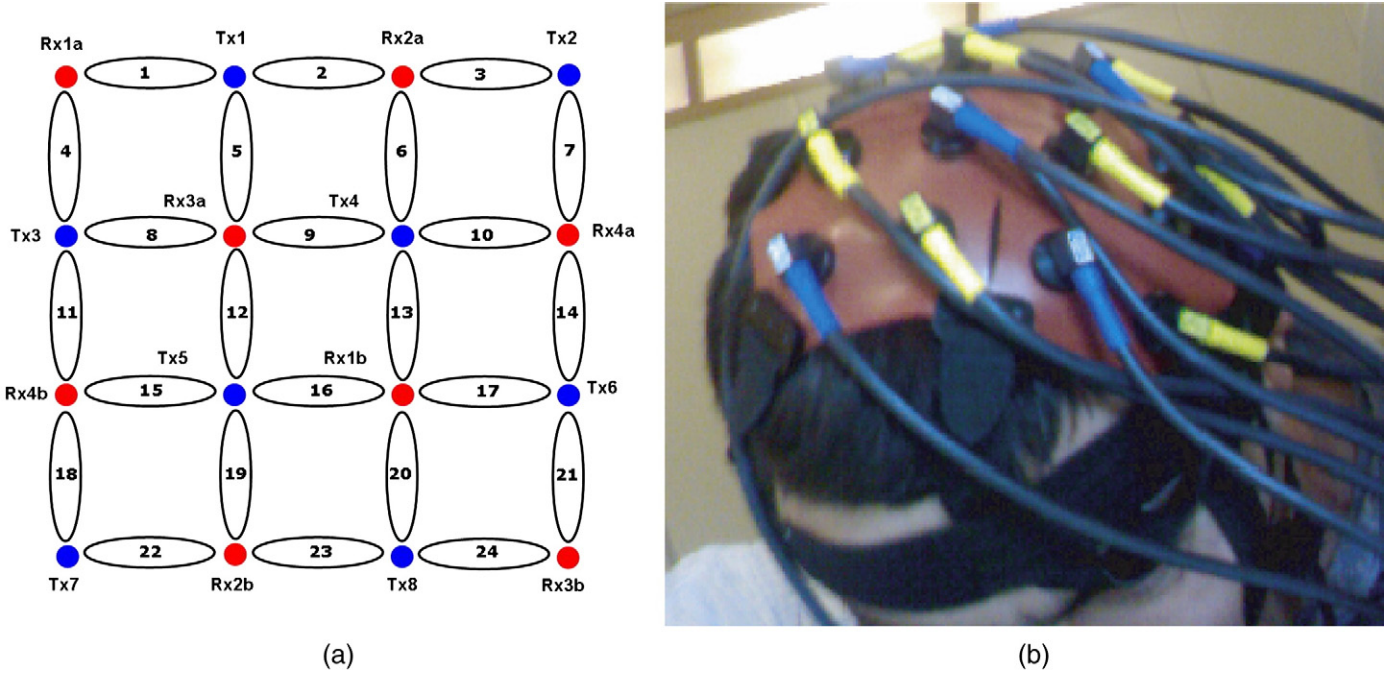


Fig. 2. (a) Schematic diagram of the 24 NIRS channels. Red circles are illuminators, and blue circles are detectors. Numbers between red and blue circles corresponds to NIRS channel index. (b) The holder cap of 16 optodes covering the primary motor cortex, dorsolateral prefrontal cortex, and Broca's area.

NIRS-fMRI alignment

In order to localize the NIRS signal with respect to the cerebral cortex of an anatomical MR image, the relationship between the MR coordinates and the real coordinates in a 3-D digitizer needs to be investigated. Horn's algorithm (Horn, 1987), which provides a closed-form and least-square solution for this absolute orientation problem, is typically employed.

Here, $p_{\text{MR},i}$ and $p_{\text{NIRS},i}$ denote a measured coordinate in the MR and 3-D digitizer system, respectively, where $i=1,2,\dots,K$ indexes the coordinates. In addition, s is a scale parameter, t is a translation vector, and \mathbf{R} is a rotation matrix. Thus, this problem seeks to find the maximum likelihood estimate for the following rigid transform parameters:

$$p_{\text{MR}} = s\mathbf{R}(p_{\text{NIRS}}) + t. \quad (27)$$

First, all measured coordinates are redefined with respect to centroids of their systems:

$$\begin{aligned} p'_{\text{MR},i} &= p_{\text{MR},i} - \bar{p}_{\text{MR}}, \\ p'_{\text{NIRS},i} &= p_{\text{NIRS},i} - \bar{p}_{\text{NIRS}}, \\ \bar{p}_{\text{MR}} &= \frac{1}{K} \sum_{i=1}^K p_{\text{MR},i}, \\ \bar{p}_{\text{NIRS}} &= \frac{1}{K} \sum_{i=1}^K p_{\text{NIRS},i}. \end{aligned} \quad (28)$$

Then, the translation vector and the scale factor are given by

$$\begin{aligned} \hat{t} &= \bar{p}_{\text{MR}} - s\mathbf{R}(\bar{p}_{\text{NIRS}}), \\ \hat{s} &= \frac{\sum_{i=1}^n p''_{\text{MR},i} \cdot R(p''_{\text{NIRS},i})}{\sum_{i=1}^n \|p''_{\text{NIRS},i}\|^2}. \end{aligned} \quad (29)$$

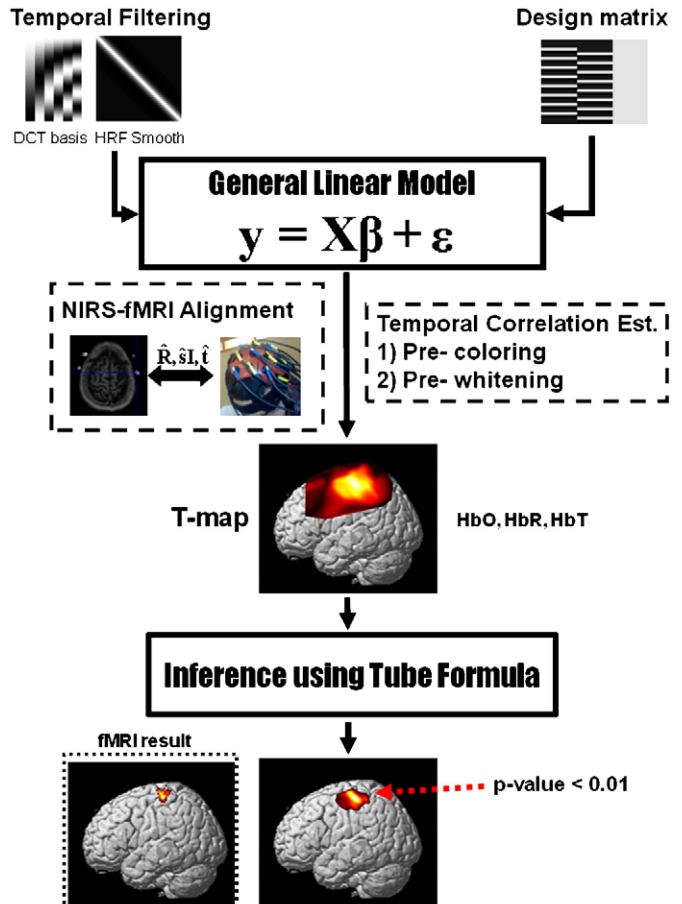


Fig. 3. Schematics describing the NIRS-SPM framework.

Let $p_i^t = (x_i^t, y_i^t, z_i^t)^T$ and

$$\mathbf{A}_{\text{MR},i} = \begin{bmatrix} 0 & -x_i^t & -y_i^t & -z_i^t \\ x_i^t & 0 & -z_i^t & y_i^t \\ y_i^t & z_i^t & 0 & -x_i^t \\ z_i^t & -y_i^t & x_i^t & 0 \end{bmatrix}, \quad \mathbf{B}_{\text{NIRS},i} = \begin{bmatrix} 0 & -x_i^t & -y_i^t & -z_i^t \\ x_i^t & 0 & z_i^t & -y_i^t \\ y_i^t & -z_i^t & 0 & x_i^t \\ z_i^t & y_i^t & -x_i^t & 0 \end{bmatrix}. \quad (30)$$

If we define the matrix \mathbf{N} as

$$\mathbf{N} = \sum_{i=1}^K \mathbf{B}_{\text{NIRS},i}^T \mathbf{A}_{\text{MR},i}. \quad (31)$$

The vector \mathbf{q} , which is directly related to the rotation parameters, is the eigenvector corresponding to the maximum eigenvalue of the

matrix \mathbf{N} . When \mathbf{q} is the quaternion $(q_0, q_x, q_y, q_z)^T$ (Korn and Korn, 1968), the rotation matrix is obtained as follows:

$$\mathbf{R} = \begin{bmatrix} (q_0^2 + q_x^2 - q_y^2 - q_z^2) & 2(q_x q_y - q_0 q_z) & 2(q_x q_z + q_0 q_y) \\ 2(q_y q_x + q_0 q_z) & (q_0^2 - q_x^2 + q_y^2 - q_z^2) & 2(q_y q_z - q_0 q_x) \\ 2(q_z q_x - q_0 q_y) & 2(q_z q_y + q_0 q_x) & (q_0^2 - q_x^2 - q_y^2 + q_z^2) \end{bmatrix} \quad (32)$$

After the relationship between the MR coordinates and real coordinates in 3-D digitizer is elicited based on the measured coordinates of marker capsules, the locations of the optodes in the MR coordinate can be calculated. Each position of the optodes is projected onto the point which has the minimum distance with cortical cortex obtained from the segmented MR images.

Preprocessing

In NIRS experiments, there often exist global drifts of the optical signal measurements for a variety of reasons, including subject

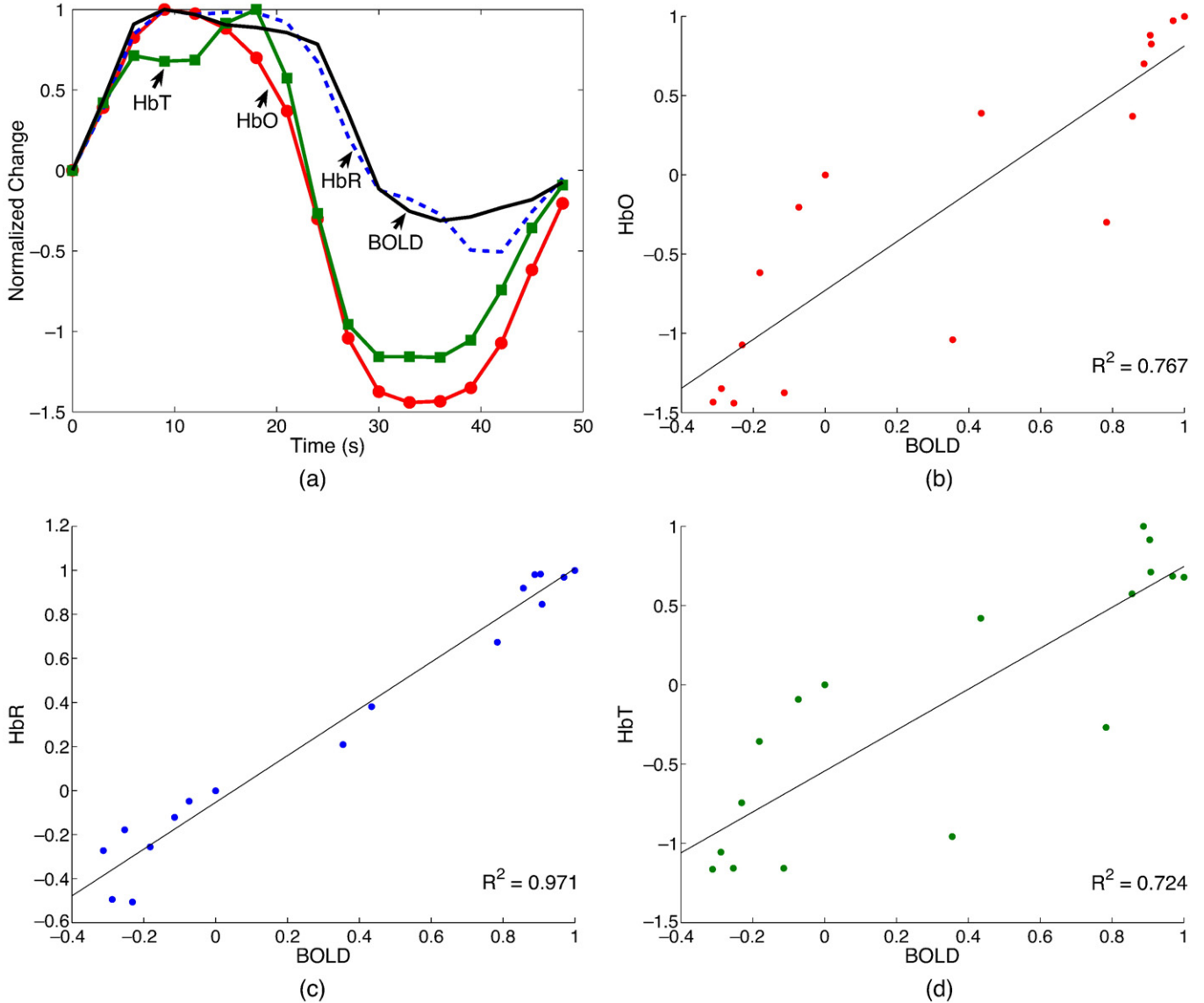


Fig. 4. (a) Ten blocks of HbO, HbR, HbT and BOLD signals from a finger tapping task are averaged to obtain average time courses. The intensity of the signals was normalized to the peak intensity, and HbR signals were inverted. HbR signal follows BOLD very closely. Correlation analysis of BOLD with (b) HbO, (c) HbR, and (d) HbT, respectively. Coefficient of determination (R^2) as well as the signal patterns between NIRS and BOLD signals shows that HbR concentration changes are highly correlated with the BOLD signal.

movement during the experiment, vasomotion, blood pressure variation, long-term physiological changes or instrumental instability. Moreover, the amplitude of the global drift is often comparable to that of the signal from a brain activation process. In order to eliminate the global trend and to improve the signal-to-noise ratio, a highpass filter based on a discrete cosine transform (DCT) was employed, as is currently implemented in SPM (Friston et al., 2006). For the NIRS data of the finger tapping task, a cutoff frequency of 1/60 Hz was used. For the NIRS data of the working memory task, a cutoff frequency of 1/128 Hz was used, as the task related frequency was 1/120 Hz.

After detrending, “short-range” temporal correlation continues to exist in NIRS data. This means that the residual signal at the specific time is correlated with its temporal neighbors. In order to obtain the correct *t*-statistics in Eq. (22), the temporal correlation structure of NIRS should be investigated. The “precoloring” method (Worsley and Friston, 1995) was compared with the “prewhitening” method (Bullmore et al., 1996; Friston et al., 2002), both initially proposed for the fMRI model (Friston et al., 2006). Currently, most of the NIRS-GLM analysis have employed the prewhitening method (Plichta et al., 2006, 2007; Koh et al., 2007; Hofmann et al., 2008). In cases where the temporal smoothing is strong enough to swamp any intrinsic temporal

correlation, the precoloring method is preferred. Specifically, if the full-width-at-half-maximum (FWHM) value of the smoothing kernel is sufficiently large, temporal correlation induced by the smoothing process can be obtained without an intrinsic temporal correlation:

$$\Lambda = \mathbf{S}\mathbf{V}\mathbf{S}^T \approx \mathbf{S}\mathbf{S}^T \quad (33)$$

Here, Λ is a temporal correlation matrix, \mathbf{V} is an intrinsic temporal correlation and \mathbf{S} is a smoothing matrix that is typically derived from the canonical HRF or Gaussian smoothing kernel (Friston et al., 2000). As the transfer function of HRF is in the frequencies of modeled neuronal signals, the canonical HRF was employed for the temporal smoothing of the NIRS time-series. An alternative way method, prewhitening involves whitening the data using the smoothing matrix \mathbf{S} that is derived from the intrinsic temporal correlation \mathbf{V} :

$$\mathbf{S} = \mathbf{K}^{-1}, \quad (34)$$

where $\mathbf{K}\mathbf{K}^T = \mathbf{V}$ and \mathbf{V} is estimated via restricted maximum likelihood (ReML) (Friston et al., 2002). If the estimated intrinsic temporal

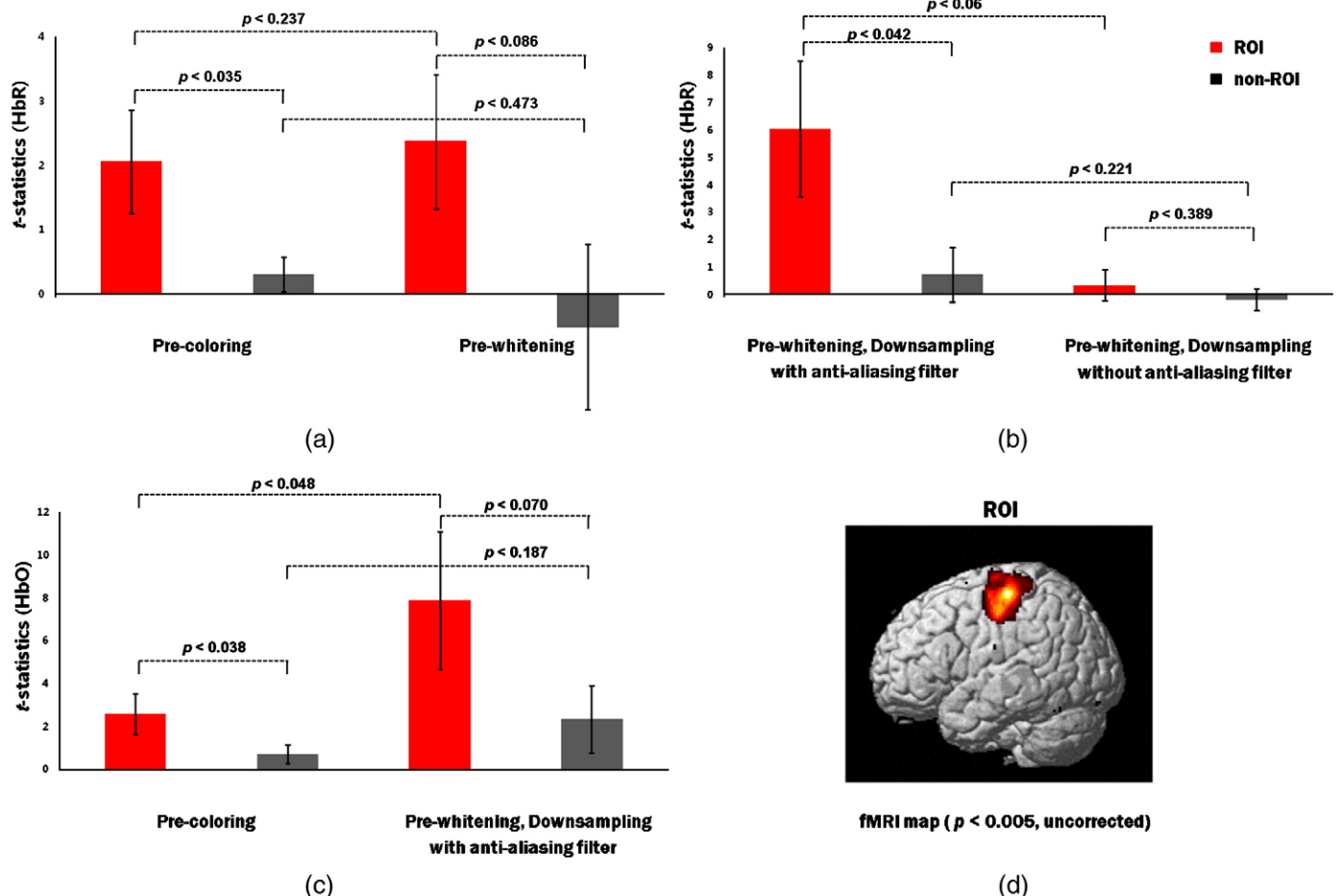


Fig. 5. (a) Paired *t*-test results to compare two paired group among the following four data sets: precolored HbR within ROI (cROI), precolored HbR outside ROI (cOUT), prewhitened HbR within ROI (wROI) and prewhitened HbR outside ROI (wOUT). (b) Paired *t*-test results to compare two paired group among the following four data sets: prewhitened HbR which is downsampled after anti-aliasing filtering within ROI (wdaROI), outside ROI (wdaOUT), prewhitened HbR which is downsampled without anti-aliasing filtering within ROI (wdROI), outside ROI (wdOUT). Downsampling factor was 10. (c) Paired *t*-test results to compare two paired group among the following four data sets: precolored HbO within ROI (cROI-HbO), precolored HbO outside ROI (cOUT-HbO), prewhitened HbO which is downsampled after anti-aliasing filtering within ROI (wdaROI-HbO), outside ROI (wdaOUT-HbO). Although significant difference was observed in cROI and cOUT ($p < 0.035$), such significant difference was not observed in wROI and wOUT ($p < 0.086$). In case of downsampled HbR, any significant difference between wdROI and wdOUT ($p < 0.389$) was not observed because of the aliasing effect. However, when the antialiasing filter was used before downsampling, a significant difference between wdaROI and wdaOUT ($p < 0.042$) was detected. Note that in case of the prewhitened HbO, no significant difference ($p < 0.070$) was observed between the *t*-map within and outside ROI, whereas the precolored HbO still provide statistically meaningful differences ($p < 0.038$). This result supports that precoloring method is superior to prewhitening method in estimating the temporal correlations. In these figures, the *t*-values indicate the averaged *t*-value within and outside ROI.

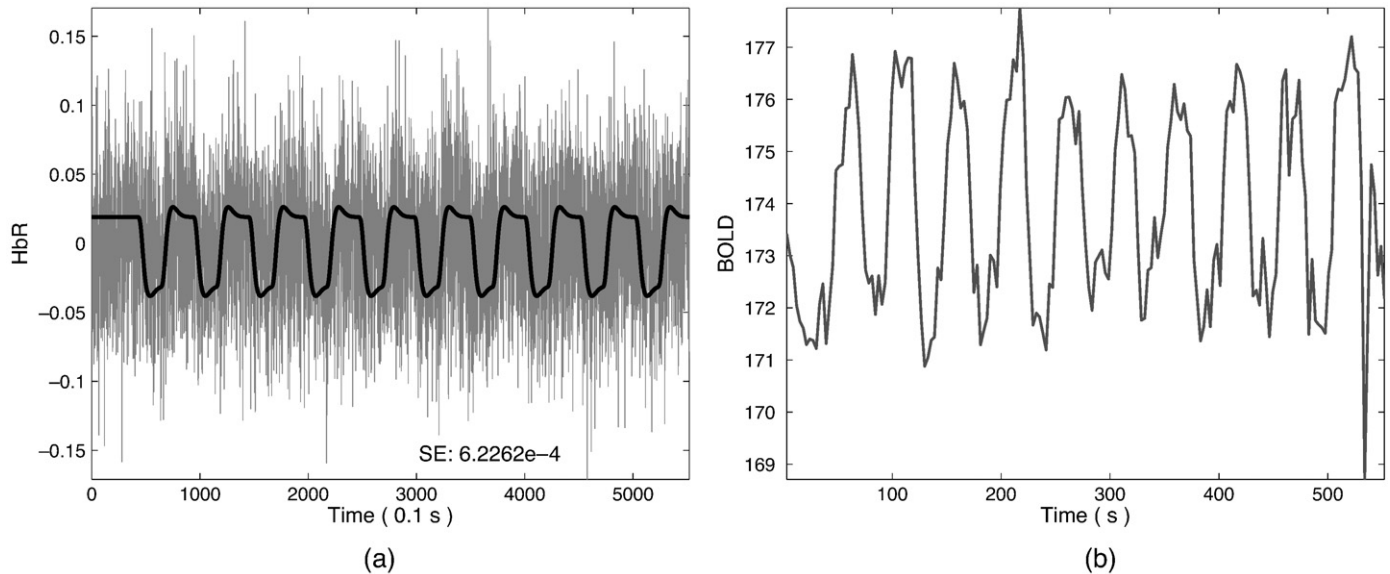


Fig. 6. (a) NIRS time series which is overlaid with the predictor model. NIRS time series was detrended using DCT basis set. The predictor model was generated by convolving the canonical HRF (+ temporal and dispersion derivatives) with the experimental protocol. Note that the predictor model adequately follows the task-related NIRS time series. (b) fMRI time series. The NIRS signal simultaneously recorded with fMRI has very low SNR, compared with the fMRI signal.

correlation is correct, the temporal correlation structure induced by smoothing can be an identity matrix, as follows:

$$\Lambda = S V S^T = I \quad (35)$$

In the whitened model, as the error is identically and independently distributed, the least-square estimate β corresponds to the maximum likelihood estimate.

Note that the spatial covariance between each channel measurement in NIRS is the result of (i) the overlap of the spatial sensitivity profiles per source-detector channel, and (ii) spatial covariance at the voxel level between hemoglobin states.³ Hence, it is assumed that all of the correlation comes from the overlapped spatial sensitivity profile as well as spatial correlation between hemoglobin states. This is in contrast with fMRI, where fMRI observations contain the assumption of no overlapping sensitivity profiles and address the spatial covariance in functional activity. One of the advantages of an SPM analysis is that such spatial covariance can be addressed during the inference step rather than during the estimation process, with the help of p -value correction with random field theory. Thus, a spatial preprocessing step for spatial covariance other than random field theory was not implemented in NIRS-SPM.

Group analysis

In fMRI, the group analysis is usually done after all the individual session data are aligned on a global template. However, the situation is different in NIRS, since there exist only a few number of optodes and the global alignments of the channel positions between individual sessions are difficult. Rather than using inter-subject alignments of optodes, this paper proposes a global alignment between the interpolated maps onto a brain template before facilitating group analysis. More specifically, the summary statistics $\hat{\chi}(r)$ of Eq. (19) and $C(r)$ of Eq. (20) are first obtained from each individual session. Since these summary statistics are already interpolated on the global template, calculating the second level statistics is quite straightforward. Methods already in use in the main statistical packages can now be used.

³ The authors acknowledge the anonymous reviewer who pointed out this issue. This sentence was borrowed from the comment of this reviewer.

More specifically, let $\hat{\chi}_{(l)}(r), l=1, \dots, L(r)$ denote the interpolated response signal from the l -th individual session, where $L(r)$ denotes the maximum number of individual sessions at position r . Note that the individual anatomical variation often results in a different $L(r)$, especially at the border areas of the maps. Let the first-level within-subject covariances be subject-specific and given by

$$C_{(l)}(r) = \left(b_{(l)}(r)^T \Sigma_{(l)} b_{(l)}(r) \right) \left(c^T \chi_{(l)}^\dagger \Lambda_{(l)} \chi_{(l)}^{TT} c \right) \quad (36)$$

where subscript (l) denotes the subject specific quantities. The between-subject variances (from the group mean) are usually modeled as equal across the group and given by σ_s^2 (Beckmann et al., 2003):

$$C_G(r) = \begin{bmatrix} C_{\chi_{(1)}}(r) & \mathbf{O} & \cdots & \mathbf{O} \\ \mathbf{O} & C_{\chi_{(2)}}(r) & \cdots & \mathbf{O} \\ \vdots & \vdots & \ddots & \vdots \\ \mathbf{O} & \mathbf{O} & \cdots & C_{\chi_{(L(r))}}(r) \end{bmatrix} + \sigma_s^2(r) I \quad (37)$$

Then, the estimate of the global parameter is given by (Beckmann et al., 2003):

$$\hat{\chi}_G(r) = \left(\mathbf{X}_G^T \mathbf{C}_G^{-1}(r) \mathbf{X}_G^T \right)^{-1} \mathbf{X}_G^T \mathbf{C}_G^{-1}(r) \hat{\chi}_l(r) = \frac{\sum_{l=1}^{L(r)} \frac{\hat{\chi}_{(l)}(r)}{C_{(l)}(r) + \sigma_s^2(r)}}{\sum_{l=1}^{L(r)} \frac{1}{C_{(l)}(r) + \sigma_s^2(r)}} \quad (38)$$

where $\mathbf{X}_G = [1 \cdots 1]^T$ denotes the design matrix for group mean activation and $\hat{\chi}_l(r) = [\hat{\chi}_{(1)}(r) \cdots \hat{\chi}_{(L(r))}(r)]$. The corresponding covariance is

$$C_{\chi_G}(r) = \left(\mathbf{X}_G^T \mathbf{C}_G^{-1}(r) \mathbf{X}_G^T \right)^{-1} = \frac{1}{\sum_{l=1}^{L(r)} \frac{1}{C_{(l)}(r) + \sigma_s^2(r)}}. \quad (39)$$

Hence, the corresponding t -statistics is given by

$$T(r) = \frac{\sum_{l=1}^{L(r)} \frac{\hat{\chi}_{(l)}(r)}{C_{(l)}(r) + \sigma_s^2(r)}}{\sqrt{\sum_{l=1}^{L(r)} \frac{1}{C_{(l)}(r) + \sigma_s^2(r)}}}, \quad (40)$$

Applying the inhomogeneous random field theory to group analysis of NIRS data is quite complicated due to the mismatch of channel positions between individual sessions. In this paper, uncorrected p -values are therefore used in group analysis of NIRS data for simplicity.

NIRS-SPM: a new SPM toolbox for NIRS

A new SPM appropriate for NIRS was implemented as a “NIRS-SPM toolbox” based on the SPM5 package (Wellcome Department of Cognitive Neurology, London, UK). The toolbox runs under MATLAB (Mathworks, Natick, MA), providing various computational processes from detrending to statistical analysis. Its statistical results are superimposed onto a 3-D rendered SPM brain map and can be compared with fMRI results, integrating the conventional SPM for fMRI. Fig. 3 shows a schematic illustrating the NIRS-SPM framework.

Experimental results

Block design analysis of right finger tapping

In order to study the correlation of hemodynamic responses of NIRS and BOLD signals, ten blocks of HbO, HbR, HbT and BOLD signals from a finger tapping task are averaged out. The intensity of the signals were normalized to the peak intensity, and HbR signals were inverted. Fig. 4a illustrates the average time courses of HbO, HbR, HbT, and BOLD concentration from nine subject NIRS data. We performed the statistical correlation analysis of oxygen species and fMRI BOLD time courses. Regression analysis shown in Figs. 4b–d indicates that BOLD is highly correlated with HbR signal ($R^2=0.971$, $p<0.001$), whereas there are relatively weak correlations between BOLD and HbO ($R^2=0.767$, $p<0.001$) and between BOLD and HbT ($R^2=0.724$, $p<0.001$), respectively.

Quantitative comparison between precoloring with prewhitening procedure was performed using the paired *t*-test. Specifically, we first defined a ROI from fMRI group activation analysis at $p=0.005$. Then, for the individual session, the *t*-statistics within the ROI and outside the ROI are separately averaged. We used the paired *t*-test to compare two paired groups among the following four data sets: precolored HbR within ROI (cROI), precolored HbR outside ROI (cOUT), prewhitened HbR within ROI (wROI) and prewhitened HbR outside ROI (wOUT). As illustrated in Fig. 5a, no significant difference was observed either

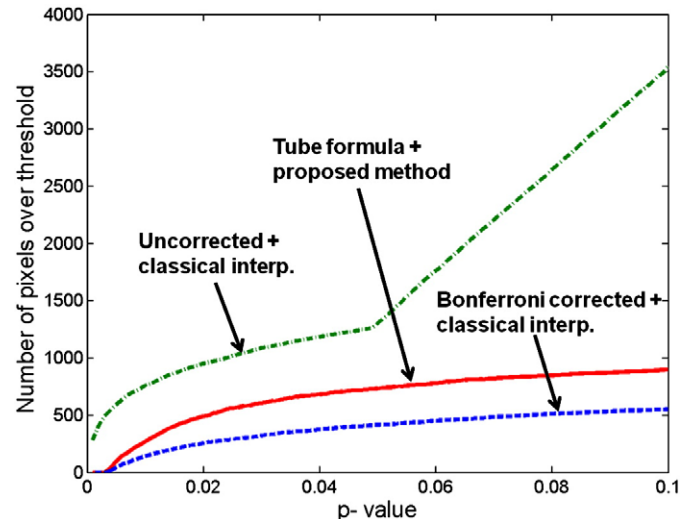


Fig. 8. The number of pixels over the threshold plotted against the *p*-values. Red line: The tube formula corrected *p*-values were applied in the *t*-statistic map obtained from the proposed method. Blue line: The Bonferroni corrected *p*-values were applied in the *t*-statistic map obtained from the classical interpolation method. Green line: The uncorrected *p*-values were applied in the *t*-statistic map obtained from the classical interpolation method. While the Bonferroni correction is too conservative and the uncorrected *p*-value is too liberal, the tube formula correction appears reasonable.

between cROI and wROI ($p<0.237$), or cOUT and wOUT ($p<0.473$). Although a significant difference was observed in cROI and cOUT ($p<0.035$), such significant difference was not observed in wROI and wOUT ($p<0.086$). The results indicated that the *t*-statistics of non-ROI in prewhitening cases has more variation than that of the precoloring method.

Next, we used the paired *t*-test to compare two paired groups among the following four data sets: prewhitened HbR which is downsampled

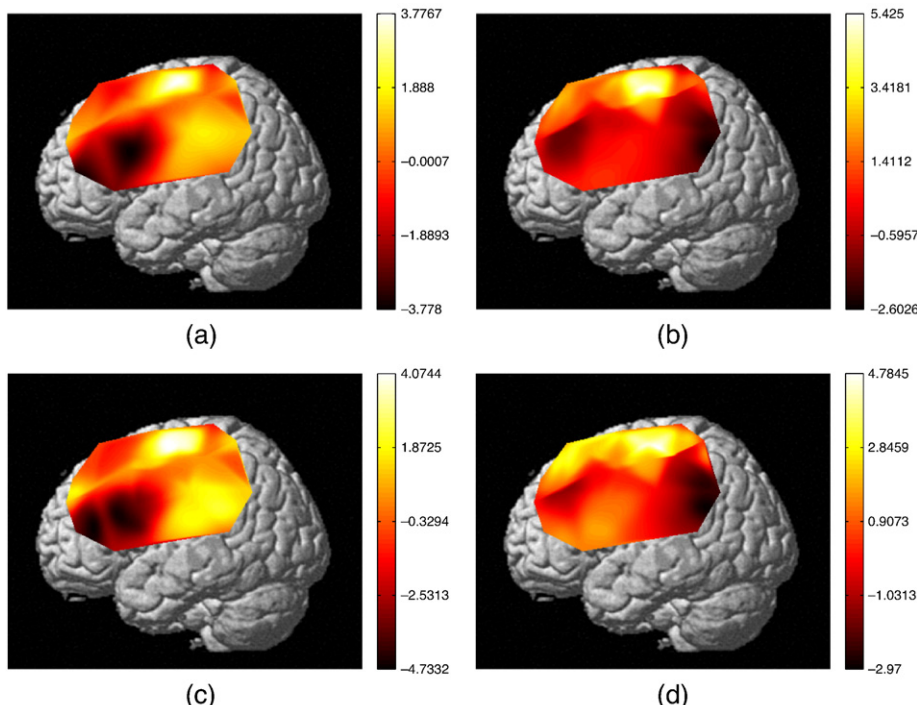


Fig. 7. Individual *t*-statistic maps from finger tapping task. (a) The *t*-statistic maps from HbR using the classical interpolation method. The *t*-statistic maps from (b) HbO, (c) HbR, and (d) HbT using NIRS-SPM. Note that the HbR-*t*-statistic values from the proposed method are higher than the HbR-*t*-statistic values from the classical interpolation.

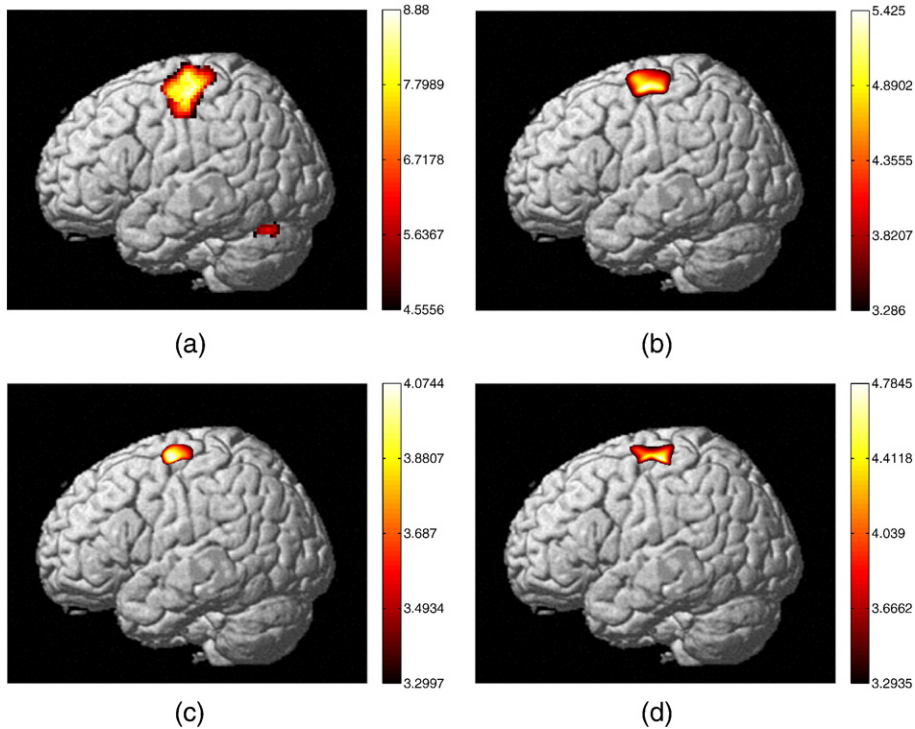


Fig. 9. Individual activation maps from finger tapping task. (a) Activation map of BOLD ($p < 0.05$, random field correction, the size of design matrix (sX) = 184×4 , the degrees of freedom $df = 172$). Activation map from (b) HbO, (c) HbR and (d) HbT using NIRS-SPM ($p < 0.05$, tube formula correction, $sX = 5384 \times 4$, $df = 82.4705$). Activation areas from HbO, HbR, and HbT are localized to the primary motor cortex very tightly and consistent with the activation areas obtained by BOLD.

after anti-aliasing filtering within ROI (wdaROI), outside ROI (wdaOUT), prewhitened HbR which is downsampled without anti-aliasing filtering within ROI (wdROI), outside ROI (wdOUT). Downsampling factor was 10. Because of the aliasing effect and low SNR, any significant difference

between wdROI and wdOUT ($p < 0.389$) was not observed. The mean t -value of wdROI was too low (0.346). However, when the anti-aliasing filter was used before downsampling, a significant difference between wdaROI and wdaOUT ($p < 0.042$) was detected.

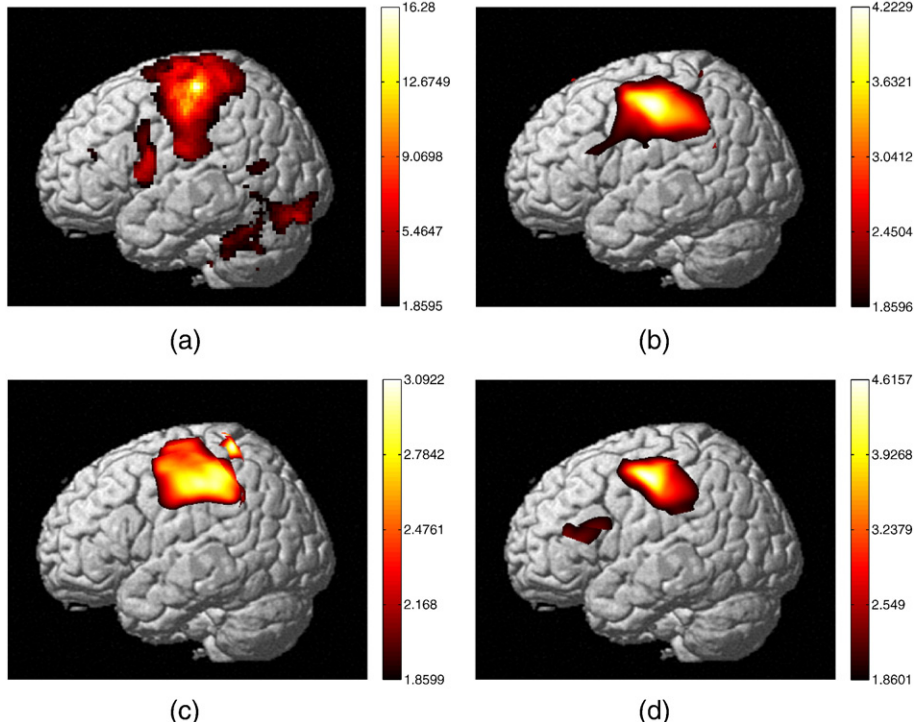


Fig. 10. Activation maps found by group analysis of finger tapping task data (9 subjects). (a) Activation map found by BOLD ($p < 0.05$, uncorrected). Activation maps found by (b) HbO, (c) HbR and (d) HbT using NIRS-SPM ($p < 0.05$, uncorrected). Activated regions found by group analysis of NIRS data are localized to the primary motor cortex. Note that activated area by HbR is more consistent with that of BOLD.

Since the precolored HbR and downsampled prewhitened HbO with anti-aliasing filter both provide the significant differences in t -maps between ROI and outside ROI ($p < 0.035$ and $p < 0.042$, respectively), we again conducted another experiment using oxy-hemoglobin species (HbO) since HbO also provides useful information about neuronal activation. Fig. 5c shows that the precolored HbO still provides statistically meaningful differences between ROI and outside ROI ($p < 0.038$), whereas no significant difference exists in the latter cases ($p < 0.07$). This result led us to choose the precoloring method.

There are several factors that can explain why precoloring is more appropriate for NIRS than prewhitening. First, sufficient temporal smoothing of the precoloring method is required in the NIRS time series as NIRS data simultaneously recorded with fMRI have a very low SNR compared to fMRI, as shown in Fig. 6. The relatively long optical fibers that connect the optode and NIRS equipment in the MRI control room account for such significant signal attenuation. Thus, in order to improve the SNR, sufficient temporal smoothing is necessary in the preprocessing step. In case of prewhitening method, the temporal smoothing matrix is derived from the intrinsic temporal correlation using unsmoothed NIRS data that have a poor SNR. These increases the probability that prewhitening produces some bias due to the difference between the estimated and actual temporal correlations. The results in Fig. 5b also confirm the importance of smoothing since the anti-aliasing filter is basically a low pass filter that improves the SNR. Second, the precoloring method obtains a temporal correlation without ReML. In ReML as employed in the prewhitening method, the precision of the hyperparameter estimates increases linearly with the number of measurements (Friston et al., 2006). As the number of channels in NIRS data is much smaller than in fMRI data, it is not feasible to estimate the intrinsic temporal correlation accurately using ReML. Furthermore, due to the computational burden of ReML, a considerable amount of time is required to obtain the estimated temporal correlation in NIRS since the number of time courses is much larger than that of fMRI. Based on these observations, the precoloring method is more appropriate for NIRS data compared to the prewhitening method. Therefore, in the sequel, we only illustrate the results from the precoloring.

In order to compensate for the individual variation, we follow Plichta et al. (2007) and construct the design matrix by including the canonical HRF, and its temporal and dispersion derivatives, and constant term. Fig. 6a shows that the estimated time course using these HRF model adequately follows the task-related NIRS signal. In

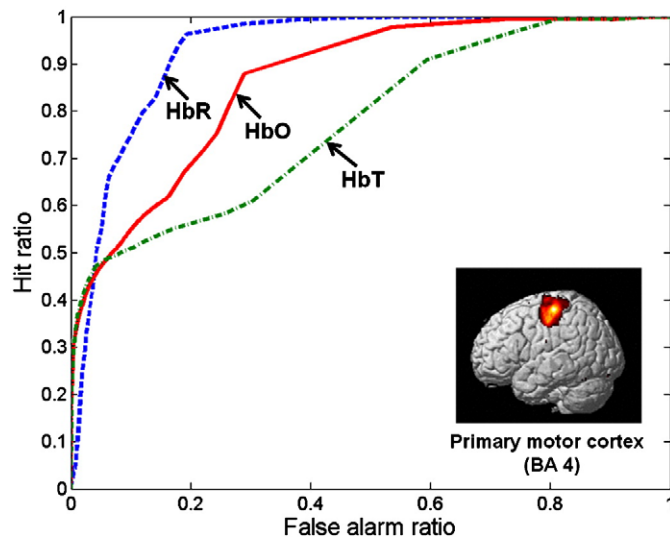


Fig. 11. Receiver operation characteristics (ROC) for HbO, HbR, and HbT. The fMRI activation map at $p = 0.005$ is used as a ground-truth, and the false alarm ratio and hit ratio are calculated by changing the threshold values for the group t -map. The ROC analysis showed that the area under the ROC curve for HbR was largest, indicating that HbR activation map can predict the BOLD activation map more reliably.

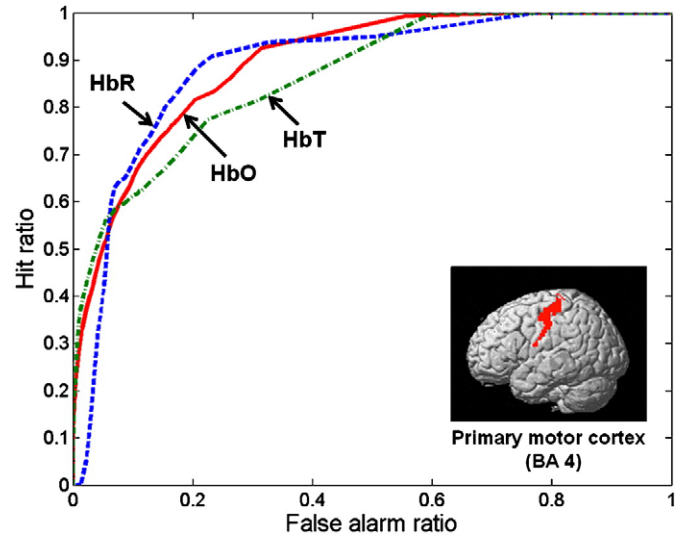


Fig. 12. Receiver operation characteristics (ROC) for HbO, HbR, and HbT. The primary motor cortex (BA4) is used as a ground-truth, and the false alarm ratio and hit ratio are calculated by changing the threshold values for the group t -map. The primary motor cortex in the SPM-brain template was depicted using the WFR PickAtlas toolbox (www.ansir.wfubmc.edu). The ROC analysis showed that the area under the ROC curve for HbR was almost same as the area under the ROC curve for HbO. This result indicated that the ratio of HbR's activation area in primary motor cortex is similar to the ratio of HbOs activation area in primary motor cortex.

order to support the superiority of the proposed method, we compared our results with that of classic interpolation technique.⁴ Fig. 7a shows a t -statistic map from HbR using the classical interpolation method. More specifically, the t -values between the channels were calculated using cubic interpolation. In contrast, the t -statistic maps from HbO, HbR, and HbT using NIRS-SPM were calculated using the optimal interpolation scheme given by Eq. (22) and illustrated in Fig. 7(b)(c)(d), respectively. Note that the t -statistic values of HbR using the proposed method are higher than that of the classical interpolation even though the t -values at each channel locations are identical. The main reason for such increases in t -statistics is that our interpolation scheme in Eq. (22) is non-linear due to the interpolated variance terms in the denominator. Furthermore, in order to address the accuracy of the tube formula for the activation detection, we compared it with the two classical methods in Fig. 8. Here, the number of pixels over the threshold is plotted against the p -values for various correction method. While the Bonferroni correction using the classical interpolation is too conservative and the uncorrected p -value is too liberal, our tube formula correction appears to be reasonable for a wide range of p -values.

Fig. 9a shows activated areas found by BOLD signal ($p < 0.05$, random field correction, the size of design matrix (sX) = 184×4 , and the effective degrees of freedom (df) = 172), which were acquired simultaneously. The activated areas are localized to the primary motor cortex very tightly. For the same subject, Figs. 9b-d show activation areas found by HbO, HbR, HbT, respectively ($p < 0.05$, tube formula correction, sX = 5384×4 , and df = 82.4705). Note that the activation areas are also localized to the primary motor cortex which is the target region of the finger tapping task. Furthermore, there is a strong correlation between the activation areas found by BOLD and by HbO, HbR, and HbT. Activation areas found by group analysis of BOLD, HbO, HbR, and HbT, are shown in Fig. 10a-d, respectively. Total number of subjects used in group analysis was nine. Again, the activated regions found by group analysis of NIRS data are fairly consistent with the BOLD result. Quantitative comparisons between NIRS and fMRI activation maps

⁴ Since fOSA cannot analyze the interpolated random field, we do not include it for comparison.

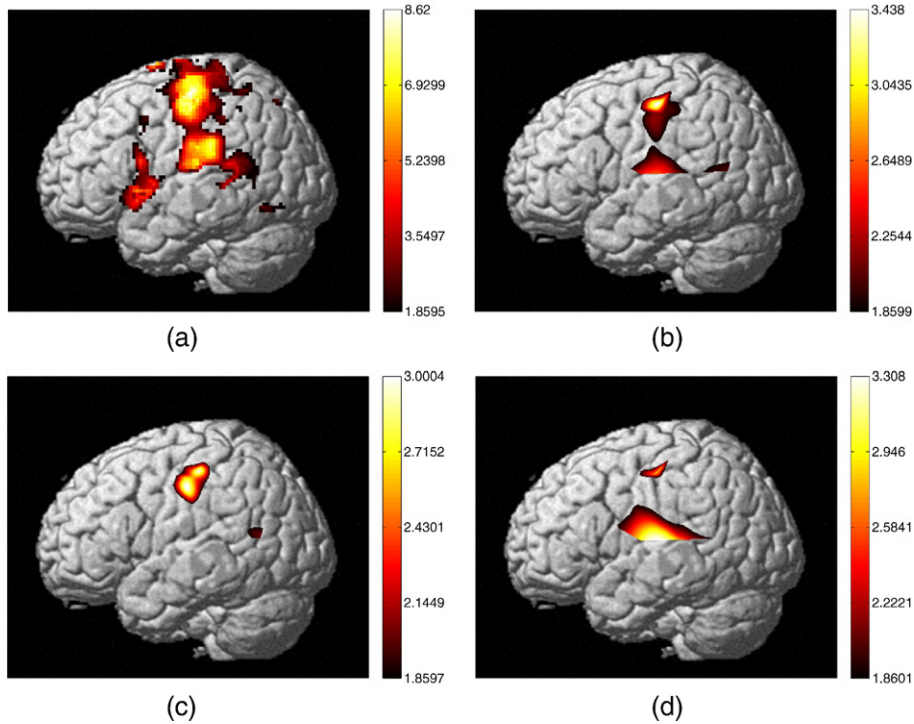


Fig. 13. Activation maps found by group analysis of event-related finger tapping task (9 subjects). Activation maps found by (a) BOLD ($p < 0.05$, uncorrected), (b) HbO, (c) HbR and (d) HbT ($p < 0.05$, uncorrected). Even though the t -value of HbR is relatively low, the activated area found by group analysis of HbR has an excellent spatial consistence with highly activated area from BOLD, compared with HbO and HbT.

were performed by calculating receiver operation characteristics (ROC) for HbO, HbR, and HbT, respectively. Since the goal of this study was to show spatial correlation between NIRS activation maps and that of fMRI, an fMRI activation map at $p = 0.005$ was used as a ground-truth in this study. Then, the false alarm ratio and hit ratio are calculated by changing the threshold values for the group analysis of

HbO, HbR, and HbT data. The ROC analysis in Fig. 11 showed that the area under the ROC curve for HbR was largest, indicating that HbR activation map can predict the BOLD activation map more reliably.

In another experiment, rather than assuming fMRI activation map as the ground-truth, the absolute coordinates of primary motor cortex (BA4) were assumed as ground-truth, and the similar experiment was

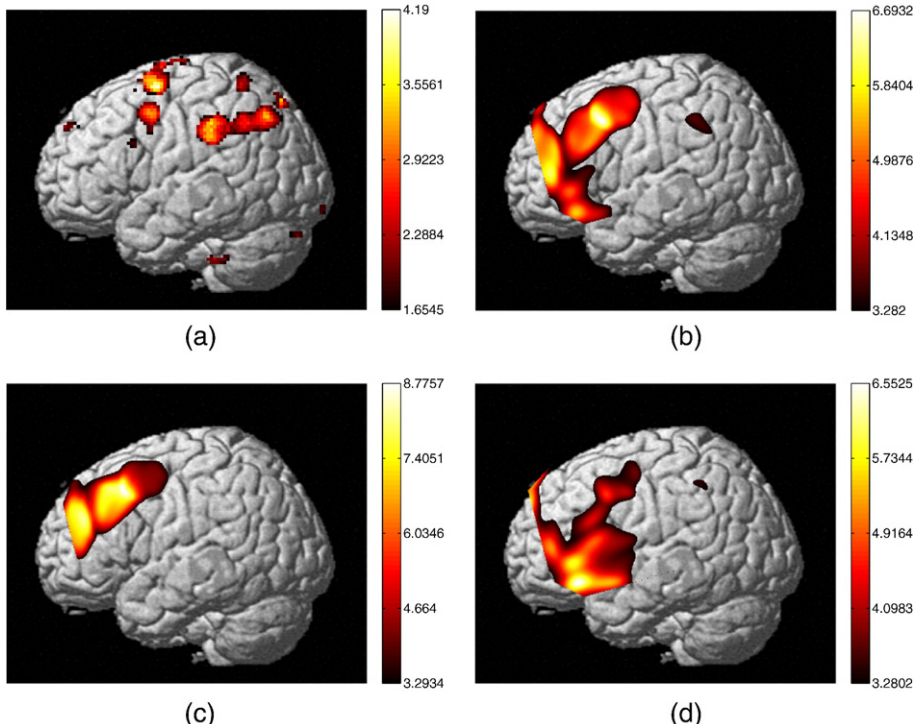


Fig. 14. Individual activation maps from working memory task. Activation maps found by (a) BOLD ($p < 0.05$, uncorrected, $sX = 174 \times 7$, $df = 159$), (b) HbO, (c) HbR and (d) HbT ($p < 0.05$, tube formula correction, $sX = 5067 \times 7$, $df = 83.8212$). Activated regions by HbO, HbR, and HbT are localized to dorsolateral prefrontal cortex and Broca's area.

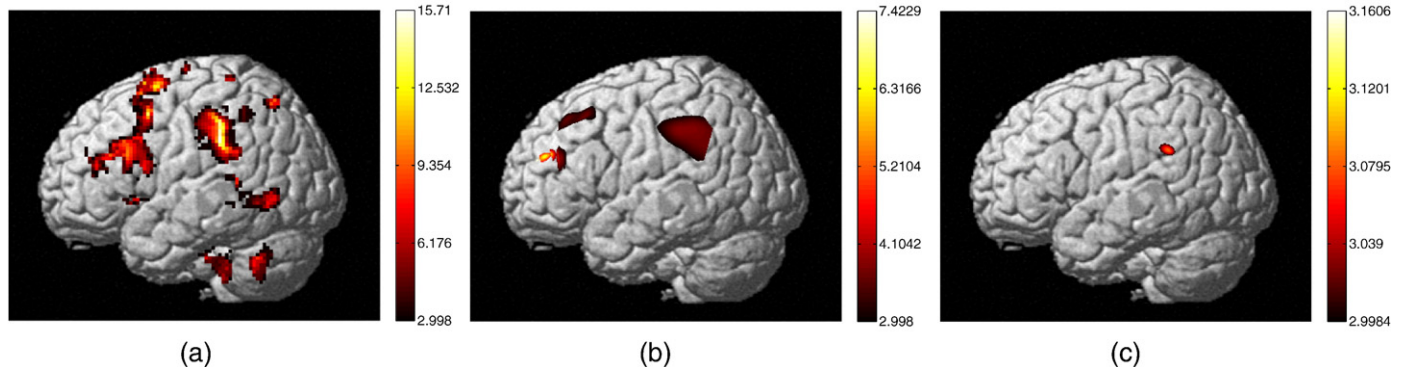


Fig. 15. Activation maps found by group analysis of working memory task (8 subjects). Activation maps found by (a) BOLD ($p<0.01$, uncorrected), (b) HbO, and (c) HbT ($p<0.01$, uncorrected).

also performed by calculating ROC for HbO, HbR and HbT, respectively. The primary motor cortex in the SPM-brain template was depicted using the WFR PickAtlas toolbox (www.ansir.wfubmc.edu). The ROC analysis in Fig. 12 showed that the area under the ROC curve for HbR was almost the same as the area under the ROC curve for HbO. This result suggests some interesting future research direction. More specifically, other oxygen species like HbO might have other information of neural activation that cannot be captured by the fMRI BOLD measurement.

Event-related right finger tapping task

In order to show the advantages of the GLM, an event-related finger tapping tasks were also performed. Figs. 13a–d show the activation maps found by group analysis of BOLD, HbO, HbR, and HbT data ($p<0.05$, uncorrected). Total number of subjects used in the group analysis was nine. Because most of the interpolated individual maps occupied the similar positions, we restricted the region of group analysis to the overlapped area of all individual subjects. Even though the t -value of HbR is relatively low, the activated area found by group analysis of HbR has an excellent spatial consistence with the activated area from BOLD, compared with HbO and HbT.

Block design working memory task

Activated areas found by BOLD ($p<0.05$, random field correction, $sX=174 \times 7$, $df=159$) using an individual subject during working memory task are shown in Fig. 14a. For the same subject, Figs. 14b–d show activation areas found by HbO, HbR, and HbT ($p<0.5$, tube formula correction, $sX=5067 \times 7$, $df=83.8212$), respectively.

Since there are many target activation regions such as dorsolateral prefrontal area, Broca's area and supplementary motor area, individual activation results are not localized to one specific area. However, still most of the activation areas are localized to dorsolateral prefrontal area and Broca's area. Fig. 15 shows the group activated regions from working memory task ($p<0.01$, uncorrected). Total number of subjects used in the group analysis was eight. Activation regions found by group analysis of BOLD, HbO, and HbT data are shown in Figs. 15a–c, respectively. Figs. 16a, b show the activated region from HbR signal and brain template overlaid with dorsolateral prefrontal cortex. The Montreal Neurological Institute (MNI) coordinate of the maximum t -value channel was $[-45.9385\ 37.1334\ 27.9298]$ and represented as the red point in Fig. 16b. Again, activated regions found by HbR signal are fairly consistent with that of BOLD signal and are localized to the dorsolateral prefrontal cortex.

Discussion

Optimal predictor for GLM

In pursuit of the optimal predictor models for HbO, HbR, and HbT, we conducted the statistical correlation analysis of their time courses and different set of predictor models. Regression analysis in Table 3 indicates that there is a strong correlation between the canonical HRF and BOLD/HbR ($R^2=0.932$ and $R^2=0.913$, respectively), but relatively a weak correlation between the canonical HRF and HbO/HbT ($R^2=0.685$ and $R^2=0.665$, respectively). If the temporal and dispersion derivatives are included, there is an increase in the correlation with HbO or HbT ($R^2=0.836$ and $R^2=0.834$, respectively). Furthermore, we

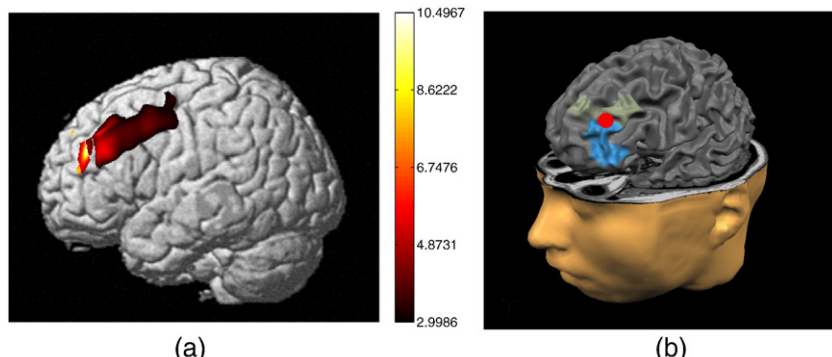


Fig. 16. (a) Activation map of HbR found by group analysis of working memory task (8 subjects, $p<0.01$, uncorrected). MNI coordinate of the channel which has the maximum t -statistics is $[-45.9385\ 37.1334\ 27.9298]$. (b) Brain template overlaid with dorsolateral prefrontal cortex region (roughly equivalent to BA 9 and BA 46). The red point denotes the channel which has the maximum t -value. Dorsolateral prefrontal cortex (BA46/9) in the brain template was depicted using the BrainVoyager software (<http://www.brainvoyager.com>). The positions of highly activated channels are overlapped with the dorsolateral prefrontal cortex.

Table 3

Correlation coefficients of low pass filtered time course with several hemodynamic response models

	cHRF	cHRF+2 deriv.	Gamma functions		
			4 basis	3 basis	2 basis
Oxy-hemoglobin	0.685	0.836	0.980	0.922	0.822
Deoxy-hemoglobin	0.913	0.942	0.977	0.942	0.942
Total- hemoglobin	0.665	0.834	0.940	0.887	0.824
fMRI BOLD	0.932	0.948	0.971	0.948	0.940

(cHRF: canonical hemodynamic response, cHRF+2 deriv.: canonical hemodynamic response with temporal and dispersion derivatives. Gamma function: gamma function fitting with different number of gamma function basis.)

observed a significant increase of the correlation if the HRF is approximated with multiple gamma function basis as shown in Figs. 17a–b. More specifically, we fixed the scale parameter of the gamma function to unity and searched a set of shape parameters as well as weighting parameters for each gamma functions:

$$\hat{h}(t) = \sum_{i=1}^p A_i t^{k_i-1} \frac{e^{-t}}{(k_i-1)!} \quad (41)$$

where $h(t)$ denotes the estimate HRF, and A_i , k_i and p are a weighting parameter, a shape parameter and a model order, respectively.

Fig. 18 shows the group activation maps from finger tapping task using HRF models of two gamma function basis. Compared with the t -statistic values from the conventional canonical HRF (Fig. 10), the t -statistic values of BOLD and HbO increased, and the activated regions from HbO and HbT are more localized to the primary motor cortex. Note that the suspicious HbT activated regions outside of the primary motor cortex in Fig. 10d are removed, as shown in Fig. 18d. We have also conducted same experiment with the HRF models using four gamma function. Nearly identical results are obtained (Figs. not shown). In working memory experiments in Fig. 19, the activated regions using HRF models with two gamma function basis also show the spatial correspondence with that from the conventional canonical HRF, and the t -statistic values are improved. Furthermore, the activated areas from HbT become more correlated with that from HbO and are localized at the target region. In Fig. 19a, the fMRI-BOLD HRF is also modeled using two gamma functions, which shows improved activation map compared to Fig. 15a.

Optimal interpolator and classical interpolation

In NIRS, only a small number of measurement channels are available from sparsely and irregularly distributed optodes. In order to acquire the activation map over whole brain cortex using NIRS, we therefore need some form of interpolation scheme.

Classically, interpolation have been performed in various domains, such as raw optical measurement domain, β parameter domain, or t -statistics, without addressing their optimality. Furthermore, we are not aware of any theoretical analysis on the optimal choice of the interpolation kernel, or systematic way of calculating the summary statistics (such as mean and variance) at the interpolated location for group analysis. While these heuristic approaches might still provide seemingly meaningful form of activation maps, the correctness of the resultant activation map is not clear.

One of the main advantages of NIRS-SPM over the classical interpolation approaches is the systematic way of optimizing the interpolation kernel and calculating the optimal statistical inference. More specifically, the main novelties of this paper are:

- to demonstrate that the optimal interpolation kernel can be obtained by considering light scattering and spatial correlation of adjacent hemoglobin states,

- to prove that the t -map should be calculated as a ratio between interpolated signal response strength and interpolated covariance, rather than direct interpolation in t -map space, or measurement space,
- to show how to calculate the “correct” p -value by considering the effect of the resultant inhomogeneous interpolation kernel.

Currently, we employ the cubic interpolator rather than fully considering light scattering model. This is because the optical parameters for brain tissue are not often available for each individual, and the optimal interpolation should take into account of spatial domain regularization since the direct inverse mapping is not stable. However, light scattering based regularized optimal interpolation scheme is by itself important and will be addressed elsewhere.

Expected Euler characteristics vs. tube formula

Mathematically, p -value can be calculated as excursion probability of underlying random fields over a threshold. Currently, two approaches are available: the expected Euler characteristics (EC) and the tube formula.

The expected EC approach has been extensively studied by Adler (Adler, 1981, 2000; Adler and Taylor, 2007), Worsley (Worsley, 1994, 1995; Cao and Worsley, 1999b) and more recently by Taylor et al.

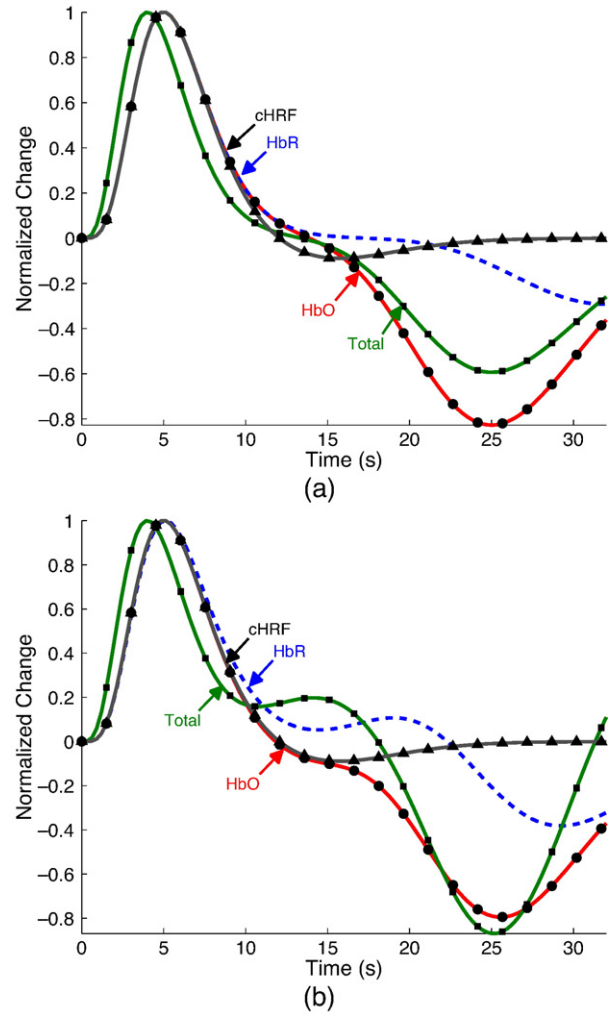


Fig. 17. Estimated hemodynamic responses for HbO, HbR, HbT, and BOLD using (a) two gamma function basis and (b) four gamma function basis. (cHRF: canonical HRF). Note that the approximated HRFs with four gamma function basis are more correlated with low pass filtered NIRS signal (See Table 3).

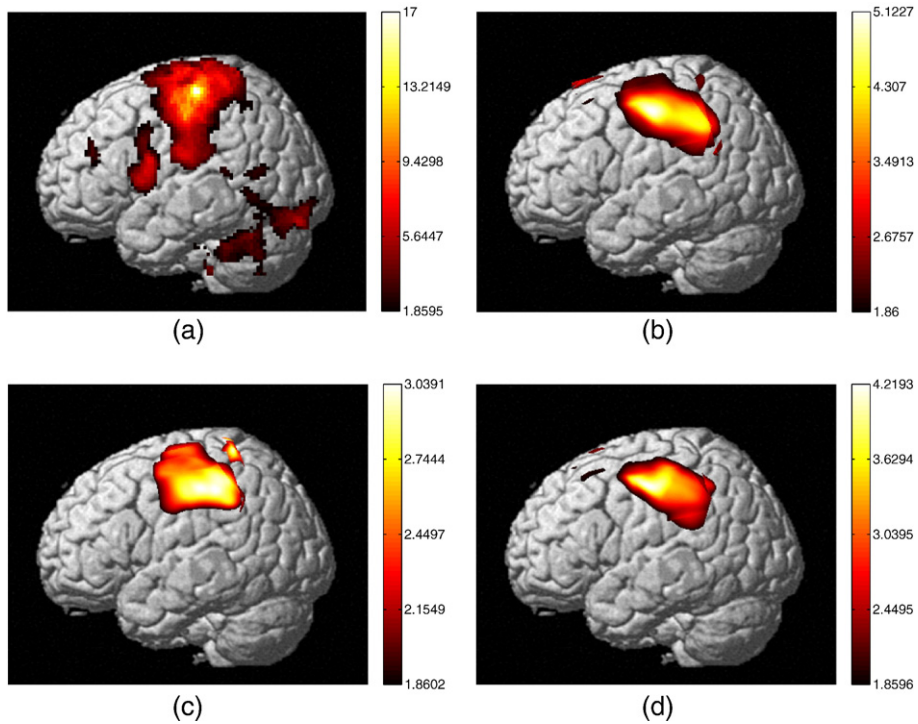


Fig. 18. Group activation maps using a HRF model of two gamma function basis (finger tapping task). Activation maps found by (a) BOLD ($p < 0.05$, uncorrected), (b) HbO, (c) HbR, and (d) HbT ($p < 0.05$, uncorrected). The t -statistic values of BOLD and HbO are slightly increased, compared with the t -values from canonical HRF. Furthermore, activated regions from HbO and HbT are more localized on the primary motor cortex. Note that suspicious HbT activation in non target area in Fig. 10(d) are now mostly removed.

(Taylor and Adler, 2003; Taylor and Worsley, 2007, 2008). A heuristic explanation of the expected EC approach for a p -value calculation is as following: if a threshold is high enough, the excursion sets over the threshold only contains isolated blobs that contain one local maximum. So the EC counts the number of excursion sets—the

quantity essential for calculating the excursion probability. The approach has been recently generalized to inhomogeneous random fields on general manifolds with boundaries. For example, in neuroscience applications, such generalization enables quantitative analysis cortical thickness variation (Taylor and Worsley, 2007).

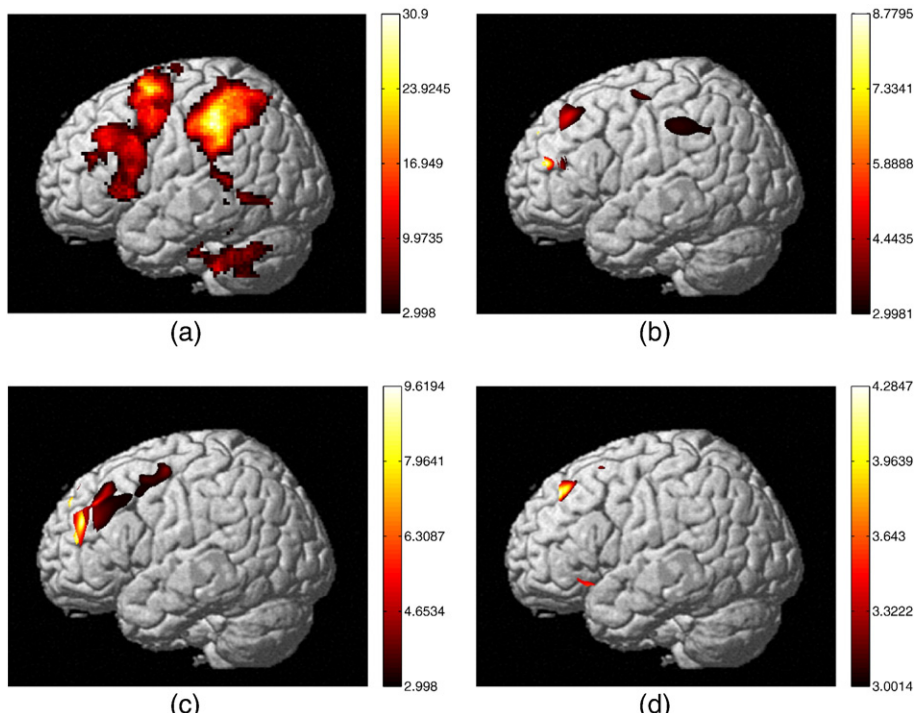


Fig. 19. Group activation maps using a HRF model of two gamma function basis (working memory task). Activation maps found by (a) BOLD ($p < 0.01$, uncorrected, $df = 7$), (b) HbO, (c) HbR, and (d) HbT ($p < 0.01$, uncorrected). The t -statistic values of BOLD, HbO, and HbT are slightly increased, compared with the t -values from canonical HRF.

Currently, major statistical packages such as fMRISTAT (available at <http://www.math.mcgill.ca/keith/fmristat/>) include inference engine based on this.

The tube formula (Johansen and Johnstone, 1990; Sun, 1993; Sun and Loader, 1994) is another approach to calculate the *p*-value of the maximum of a random field. As described in Appendix D, the tube formula is based on the finite expansion of Karhunen–Loeve expansion of the random field, whose basis functions consist of independent zero mean unit variance Gaussian random variables. Then, the *p*-value of the maximum of the first m terms of the Karhunen–Loeve expansion corresponds to ratio of the measure of a “tube” to the measure of the m -dimensional unit sphere, where the radius of the tube depends on the threshold of the random field. The tube formula does not assume any isotropy; hence, it can be applied to inhomogeneous Gaussian random fields. Furthermore, according to Taylor and Worsley (2008), “in an unpublished manuscript by Sun, it was generalized to include more general boundary cases”. In the case of Gaussian random fields, Takemura and Kuriki (2002) show that the tube formula and the expected EC essentially give the same results.

The expected EC approach can be now applied to non-Gaussian random fields such as *t*- and *F*-statistics with the help of the union-intersection principle (Taylor and Worsley, 2008). However, the application of union-intersection principle to the tube formula may appear difficult in general since the required high dimensional embedding may complicate the Karhunen–Loeve expansion of the resultant higher dimensional random fields.

Interestingly, for the case of interpolated random fields described in NIRS-SPM, Appendix D shows that the union-intersection trick can be still applied to calculate the excursion probability of the *t*-statistic without altering the finiteness of Karhunen–Loeve expansion. Furthermore, *p*-value can be calculated directly using the close form expression of the derivatives of the basis and the noise covariance matrix, without resorting to the mesh map as in the expected EC approach. Hence, even though the two approaches provide the essentially same *p*-values, the tube formula appears easier for NIRS-SPM.

Stand-alone NIRS vs. simultaneous fMRI/NIRS

In most of the cases when no MRI record is available, one will place the optodes with *a priori* knowledge and may define ROIs based on their localization. Here no information of interpolation will enter the calculated mean values.⁵ For these stand-alone applications, the accurate localization property of NIRS-SPM may not be noticeable since the exact location of the optodes are not available. However, if a separately acquired MR image can provide the MNI coordinate of each optode, NIRS-SPM can still provide useful spatial information of the activation map. Furthermore, the recent study (Tsuzuki et al., 2007) showed that the spatial registration of stand-alone NIRS data onto MNI space without any anatomical information of MRI. If exact optode positions in MNI space can be obtained, NIRS-SPM framework is still useful for obtaining the high resolution activation maps.

The effective degrees of freedom

In order to calculate the *p*-value of the *t*-statistics using Sun's tube formula, *t*-statistics should be reasonably approximated by the *z*-score. How well the *t*-statistics is approximated by the *z*-score is determined by the degrees of freedom. The larger the degrees of freedom are, the better the *z*-approximation of the *t*-statistics. As shown in Figs. 6a,b, the length of NIRS time series ($N>5000$) is significantly larger than that of fMRI time series ($N>183$), implying

significantly large degree of freedom. However, the existence of temporal correlations decreases the effective degrees of freedom defined by Eq. (23). From this perspective, the precoloring method is not as effective as prewhitening method in providing large effective degrees of freedom ($df=82.47$ vs $df=5364$ for finger tapping experiment), since the resultant temporal correlation of precoloring is mainly dominated by the canonical HRF filter (see Eq. (55) for the exact expression of serial correlation). However, the experimentally measured effective degrees of freedom by the precoloring is still in a reasonable range considering that Worsley and Friston (1995) indicated the *z*-approximation of *t*-statistics is accurate as long as $df>40$.

Conclusion

A new public domain statistical toolbox known as NIRS-SPM is introduced in this study. In the main framework, NIRS-SPM successfully analyzed NIRS data using GLM and calculated the *p*-value as the excursion probability for an inhomogeneous Gaussian random field that is interpolated from sparsely distributed measurements. When estimating the temporal correlation of NIRS, it was found that the precoloring method is more appropriate for NIRS compared to the prewhitening method due to the sufficient temporal smoothing and computational efficiency of this method. In the spatial preprocess, NIRS-SPM accurately localized the NIRS signal onto the cerebral cortex of an anatomical MR image using Horn's algorithm. Experimental results from right finger tapping and working memory tasks showed that the activation pattern of NIRS from the proposed software program was fairly consistent with that of fMRI. Furthermore, NIRS-SPM allowed superresolution localization of the activated area.

Acknowledgments

This research was supported by the Brain Neuroinformatics Research program by Korean Ministry of Knowledge Economy. The authors would like to thank Prof. Yong Jeong at KAIST for the valuable input into the design of the paradigm.

Appendix A

For given wavelength λ_1 and λ_2 , Eq. (6) can be represented by

$$\begin{bmatrix} \Delta\phi(r,s;\lambda_1,t) \\ \Delta\phi(r,s;\lambda_2,t) \end{bmatrix} \simeq \begin{bmatrix} \int dr' \frac{U_0(r,r';\lambda_1)U_0(r',s;\lambda_1)}{U_0(r,s;\lambda_1)} \Delta\mu_a(r';\lambda_1,t) \\ \int dr' \frac{U_0(r,r';\lambda_2)U_0(r',s;\lambda_2)}{U_0(r,s;\lambda_2)} \Delta\mu_a(r';\lambda_2,t) \end{bmatrix}. \quad (42)$$

One of the basic assumption of NIRS is that other than oxy- and deoxy-hemoglobin variation, the optical parameters are independent of the wavelength; hence, the corresponding Green's function is identical, i.e. $U_0(r,r';\lambda_1)=U_0(r,r';\lambda_2)$. In such a case, the following holds:

$$\begin{bmatrix} \Delta\phi(r,s;\lambda_1,t) \\ \Delta\phi(r,s;\lambda_2,t) \end{bmatrix} \simeq \int dr' \frac{U_0(r,r';\lambda_1)U_0(r',s;\lambda_1)}{U_0(r,s;\lambda_1)} \begin{bmatrix} \Delta\mu_a(r';\lambda_1,t) \\ \Delta\mu_a(r';\lambda_2,t) \end{bmatrix} \quad (43)$$

Multiplying the inverse of the extinction coefficient matrix that is similar to Eq. (2) results in the optical density variation with respect to the HbX variation:

$$\Delta\phi_{\text{HbX}}(r,s;t) \simeq \int dr' \frac{U_0(r,r';\lambda_1)U_0(r',s;\lambda_1)}{U_0(r,s;\lambda_1)} \Delta c_{\text{HbX}}(r';t) \quad (44)$$

where HbX denotes HbO or HbR. As the mapping from $\Delta c_{\text{HbX}}(r';t)$ to $\Delta\phi_{\text{HbX}}(r,s;t)$ is compact, stable inverse operator does not exist. If we take into consideration of the spatial correlation of adjacent

⁵ The authors acknowledge the anonymous reviewer who pointed out this issue. This sentence was borrowed from the comment of this reviewer.

hemoglobin states, a regularized inverse mapping $B(r';r,s)$ exists and is given by:

$$\Delta c_{\text{HbX}}(r';t) \approx \int \int dr ds B(r';r,s) \Delta \phi_{\text{HbX}}(r,s;t) \quad (45)$$

Given that the number of detector and source combinations is equal to the channel number K , Eq. (45) can be written in summation form:

$$\Delta c_{\text{HbX}}(r';t) \approx \sum_{i=1}^K B_i(r') \Delta \phi_{\text{HbX}}(r_i, s_i; t) \quad (46)$$

where $B_i(r') = B(r';r_i, s_i)$ corresponds to the inhomogeneous interpolation kernel.

Appendix B

The following properties of the Kronecker product \otimes are often used (Jain, 1989):

$$(\mathbf{A} \otimes \mathbf{B})^T = (\mathbf{A}^T \otimes \mathbf{B}^T) \quad (47)$$

$$(\mathbf{A} \otimes \mathbf{B})^{-1} = (\mathbf{A}^{-1} \otimes \mathbf{B}^{-1}) \quad (48)$$

$$(\mathbf{A} \otimes \mathbf{B})(\mathbf{C} \otimes \mathbf{D}) = (\mathbf{A}\mathbf{C} \otimes \mathbf{B}\mathbf{D}). \quad (49)$$

Then, the least-square estimation of β is given by

$$\hat{\beta} = (\mathbf{I}_K \otimes \mathbf{X})^\dagger \mathbf{y} = (\mathbf{I}_K \otimes \mathbf{X}^\dagger) \mathbf{y} \quad (50)$$

where $\mathbf{X}^\dagger = (\mathbf{X}^T \mathbf{X})^{-1} \mathbf{X}^T$ denotes the pseudo-inverse of \mathbf{X} . The corresponding estimation error covariance matrix is then given by

$$\mathbf{C}_{\hat{\beta}} = E[\hat{\beta} \hat{\beta}^H] = (\mathbf{I}_K \otimes \mathbf{X}^\dagger) E[\mathbf{y} \mathbf{y}^H] (\mathbf{I}_K \otimes \mathbf{X}^{T\dagger}) = (\mathbf{I}_K \otimes \mathbf{X}^\dagger) \mathbf{C}_\epsilon (\mathbf{I}_K \otimes \mathbf{X}^{T\dagger}). \quad (51)$$

In an estimation of the error covariance matrix, SPM assumes that the temporal correlation matrix is identical at all voxels, but the variance is different (Friston et al., 2006). Hence, the error covariance matrix at the i th channel is given by:

$$\mathbf{C}_{\epsilon^{(i)}} = E[\epsilon^{(i)} \epsilon^{(i)\top} T] = (\sigma^{(i)})^2 \mathbf{\Lambda} \quad (52)$$

where $\mathbf{\Lambda}$ is the temporal correlation matrix and $(\sigma^{(i)})^2$ denotes the variance, respectively. The variance $(\sigma^{(i)})^2$ at the i th channel can be estimated using the usual estimator in a least squares mass-univariate scheme:

$$(\sigma^{(i)})^2 = \frac{\mathbf{y}^{(i)\top} \mathbf{R} \mathbf{y}^{(i)}}{\text{trace}(\mathbf{R} \mathbf{\Lambda})}, \quad (53)$$

where $\mathbf{R} = \mathbf{I} - \mathbf{X}(\mathbf{X}^T \mathbf{X})^{-1} \mathbf{X}^T$ is the residual forming matrix (Worsley and Friston, 1995).

Based on this model, the following holds:

$$\mathbf{C}_\epsilon = \begin{bmatrix} \sigma^{(1)^2} \mathbf{\Lambda} & \mathbf{O} & \cdots & \mathbf{O} \\ \mathbf{O} & \sigma^{(2)^2} \mathbf{\Lambda} & \cdots & \mathbf{O} \\ \vdots & \vdots & \ddots & \vdots \\ \mathbf{O} & \mathbf{O} & \cdots & \sigma^{(K)^2} \mathbf{\Lambda} \end{bmatrix} = \Sigma \otimes \mathbf{\Lambda} \quad (54)$$

where

$$\Sigma = \begin{bmatrix} \sigma^{(1)^2} & \mathbf{O} & \cdots & \mathbf{O} \\ \mathbf{O} & \sigma^{(2)^2} & \cdots & \mathbf{O} \\ \vdots & \vdots & \ddots & \vdots \\ \mathbf{O} & \mathbf{O} & \cdots & \sigma^{(K)^2} \end{bmatrix} \quad (55)$$

Therefore, the final form of the error covariance matrix is given by

$$\mathbf{C}_{\hat{\beta}} = (\mathbf{I}_K \otimes \mathbf{X}^\dagger)(\Sigma \otimes \mathbf{\Lambda})(\mathbf{I}_K \otimes \mathbf{X}^{T\dagger}) = \Sigma \otimes (\mathbf{X}^\dagger \mathbf{\Lambda} \mathbf{X}^{T\dagger}) \quad (56)$$

Appendix C

In this section, the GLM model is derived for $\Delta c_{\text{HbX}}(r;t)$ in Eq. (46). Stacking $\{\Delta c_{\text{HbX}}(r;t_i)\}_{i=1}^N$ into a vector $\Delta \mathbf{c}_{\text{HbX}}(r)$ gives the following:

$$\Delta \mathbf{c}_{\text{HbX}}(r) = (\mathbf{b}(r)^T \otimes \mathbf{I}_N) \mathbf{y}. \quad (57)$$

Here, $\mathbf{b}(r)$ denotes the basis vector given in Eq. (17) and \mathbf{y} is given by Eq. (11), respectively. The GLM model is then given by

$$\Delta \mathbf{c}_{\text{HbX}}(r) = (\mathbf{b}(r)^T \otimes \mathbf{I}_N) \mathbf{y} = (\mathbf{I}_K \otimes \mathbf{X}) \alpha(r) + \epsilon. \quad (58)$$

Then, with the property of the Kronecker delta product, the following is true:

$$\hat{\alpha}(r) = (\mathbf{b}^T \otimes \mathbf{X}^\dagger) \Delta \mathbf{c}_{\text{HbX}}(r) = (\mathbf{b}^T \otimes \mathbf{I}_N)(\mathbf{I}_K \otimes \mathbf{X}^\dagger) \Delta \mathbf{c}_{\text{HbX}}(r) = (\mathbf{b}(r)^T \otimes \mathbf{I}_N) \hat{\beta} \quad (59)$$

This implies that the response signal strength for the interpolated measurement is equivalent to the interpolated response signal strength with the same interpolation kernel. Similarly, it is possible to obtain the error covariance matrix for $\hat{\alpha}$

$$\begin{aligned} \mathbf{C}_{\hat{\alpha}} &= (\mathbf{b}(r)^T \otimes \mathbf{I}_N) \mathbf{C}_\beta (\mathbf{b} \otimes \mathbf{I}_N) \\ &= (\mathbf{b}(r)^T \Sigma \mathbf{b}(r)^T) \otimes (\mathbf{X}^\dagger \mathbf{\Lambda} \mathbf{X}^{T\dagger}). \end{aligned} \quad (60)$$

Appendix D

Here, the p -value of the t -statistics to abandon null hypothesis is given by:

$$p = P\left\{\max_{r \in \Psi} |T(r)| \geq z\right\} = \frac{1}{2} P\left\{\max_{r \in \Psi} |T(r)|^2 \geq z^2\right\} \quad (61)$$

due to the symmetry of the $T(r)$ around zero. Furthermore, the following equalities hold:

$$\begin{aligned} P\left\{\max_{r \in \Psi} |T(r)|^2 \geq z^2\right\} &= P\left\{\max_{r \in \Psi} (\mathbf{c}^T \hat{\alpha}(r))^T \mathbf{C}_\beta (\mathbf{c}^T \hat{\alpha}(r)) \geq z^2\right\} \\ &= P\left\{\max_{r \in \Psi} \hat{\beta}^T \mathbf{B}(r) (\mathbf{B}(r)^T \mathbf{C}_\beta^{-1} \mathbf{B}(r))^{-1} \mathbf{B}(r)^T \hat{\beta} \geq z^2\right\} \\ &= P\left\{\max_{r \in \Psi} \mathbf{Z}^T \mathbf{C}_\beta^{1/2} \mathbf{B}(r) (\mathbf{B}(r)^T \mathbf{C}_\beta^{-1} \mathbf{B}(r))^{-1} \mathbf{B}(r)^T \mathbf{C}_\beta^{1/2} \mathbf{Z} \geq z^2\right\} \\ &= P\left\{\max_{r \in \Psi} \mathbf{Z}^T \mathbf{P}(r) \mathbf{Z} \geq z^2\right\} \end{aligned} \quad (62)$$

where

$$\mathbf{B} \triangleq \mathbf{c}^T (\mathbf{b}(r)^T \otimes \mathbf{I}_N) \quad (63)$$

$$\mathbf{Z} \triangleq \mathbf{C}_\beta^{1/2} \hat{\beta} \in \mathbb{R}^{KM}$$

$$\mathbf{P}(r) \triangleq \mathbf{C}_\beta^{1/2} \mathbf{B}(r) (\mathbf{B}(r)^T \mathbf{C}_\beta^{-1} \mathbf{B}(r))^{-1} \mathbf{B}(r)^T \mathbf{C}_\beta^{1/2} \quad (64)$$

where $Z \sim N(\mathbf{0}, \mathbf{I}_{KM})$ denotes the zero-mean independent Gaussian random vector and $\mathbf{P}(r)$ is the $KM \times KM$ projection matrix onto the range space of $\mathbf{C}_\beta^{1/2} \mathbf{B}(r)$, which is well defined for all $r \in \Psi$. Hence, using Eqs. (19) and (20), the following decomposition holds true:

$$\mathbf{P}(r) = \mathbf{u}(r) \mathbf{u}(r)^T. \quad (65)$$

The unit vector \mathbf{u} in this case is given by

$$\mathbf{u} = \frac{\hat{\mathbf{C}}_{\beta, HbO_2}^{1/2} (\mathbf{b}(r)^T \otimes \mathbf{I}_M) \mathbf{c}}{\sqrt{(\mathbf{b}(r)^T \Sigma \mathbf{b}(r))} \sqrt{(\mathbf{c}^T \mathbf{X}^\dagger \Lambda \mathbf{X}^T \mathbf{c})}} \quad (66)$$

The excursion probability in Eq. (62) can be calculated using the excursion probability of the zero-mean unit variance inhomogeneous Gaussian random field:

$$p = \frac{1}{2} P \left\{ \max_{r \in \Psi} \mathbf{Z}^T \mathbf{P}(r) \mathbf{Z} \geq z^2 \right\} = P \left\{ \max_{r \in \Psi} \chi(r) \geq z \right\}. \quad (67)$$

where the excursion probability of a non-Gaussian random field can be converted into a Gaussian random field using the similar technique in Taylor and Worsley (2008):

$$\chi(r) = \mathbf{u}(r)^H \mathbf{Z}. \quad (68)$$

At this point, inhomogeneous Gaussian random field theory such as expected EC (Taylor and Adler, 2003; Taylor and Worsley, 2007, 2008) or tube formula (Sun, 1993; Cao and Worsley, 1999b) can be applied to calculate the p -value. In this paper, we prefer the tube formula thanks to the finite Karhunen–Loeve expansion of the resultant covariance matrix.

More specifically, a case in which Ψ is a compact subset of \mathbb{R}^N and $X(r), r \in \Psi$ is a non-singular Gaussian random field with zero mean, unit variance, and covariance function $C_X(r, r')$ is considered. If $C_X(r, r')$ has finite Karhunen–Loeve expansion

$$C_X(r, r') = \sum_{i=1}^M u_i(r) u_i(r'), \quad (69)$$

and the manifold $U = \{[u_1(r), \dots, u_M(r)]^T, r \in \Psi\}$ has no boundary, then

$$P \left\{ \sup_{r \in \Psi} \chi(r) \geq z \right\} = \kappa_0 \psi_0(z) + \dots + \kappa_{\tilde{D}} \psi_{\tilde{D}}(z) + o(\psi_{\tilde{D}}(z)) \quad (70)$$

where $\tilde{D} = D$ for an even value of D and $\tilde{D} = D - 1$ for an odd value of D , respectively. Here

$$\psi_n(z) = \frac{1}{2^{1+n/2} \pi^{(D+1)/2}} \int_{z^{2/2}}^{\infty} u^{(D+1-n)/2-1} e^{-u} du, \quad (71)$$

where $n = 0, 2, \dots, \tilde{D}$. In Eq. (70), $\kappa_0, \dots, \kappa_{\tilde{D}}$ are the constants in Weyl's formula (Weyl, 1939) for the manifold U .

Interestingly, the covariance matrix for Eq. (68) can be simply represented as a finite Karhunen–Loeve expansion:

$$C_X(r, r') = \sum_{i=1}^{KM} u_i(r) u_i(r') \quad (72)$$

where $u_i(r)$ denotes the i -th elements of $\mathbf{u}(r) \in \mathbb{R}^{KM}$. Therefore, Sun's tube formula can be utilized. While $\kappa_0, \dots, \kappa_{\tilde{D}}$ are important constants from Weyl's formula, the most important constant to calculate simply is κ_0 . This constant is related to the metric tensor of the manifold U :

$$R(r) \triangleq E[\nabla \chi(r) \nabla^T \chi(r)] \quad (73)$$

and

$$\kappa_0 = |\mathcal{U}| = \int_{\Psi} \sqrt{|\det(R(r))|} dr \quad (74)$$

Therefore, the p -value for the activation map can be approximated by

$$p = P \{ \max_{r \in \Psi} T(r) \geq z \} \approx \frac{\kappa_0}{\omega_D} \left(1 - \Gamma \left(\frac{D+1}{2}, \frac{z^2}{2} \right) \right) [1 + O(z^{-2})] \quad (75)$$

where κ_0 is given by Eq. (74) and

$$\omega_D = \frac{2\pi^{(D+1)/2}}{\Gamma \left(\frac{D+1}{2} \right)} \quad (76)$$

denotes the surface area of the $(D+1)$ -dimensional unit sphere, and the incomplete Gamma function as

$$\Gamma(a, \chi) = \frac{1}{\Gamma(a)} \int_0^{\chi} e^{-y} y^{a-1} dy, \quad a \in \mathbb{R}, \chi \geq 0. \quad (77)$$

Here, $\Gamma(1/2) = \sqrt{\pi}$ and $\Gamma(a+1) = a\Gamma(a)$. Using the asymptotic formula for the incomplete gamma function

$$1 - \Gamma(a, \chi) \sim \frac{1}{\Gamma(a)} \chi^{a-1} e^{-\chi} \quad \text{as } \chi \rightarrow \infty. \quad (78)$$

for $D=3$ the following equation can be derived:

$$p \sim \frac{\kappa_0}{(2\pi)^2} z^2 \exp \left(-\frac{z^2}{2} \right). \quad (79)$$

This implies that the present formula is an extension of the homogenous Gaussian random field formula due to the equality $\kappa_0 = V|\Lambda|^{-1/2}$ for homogeneous Gaussian random field, where V is the volume and Λ denotes the 3×3 variance matrix of the partial derivatives of the underlying Gaussian random field.

In real measurement scenario, the interpolation function $B_i(r)$ is three-dimensional, i.e. $\Psi \subset \mathbb{R}^3$ and $D=3$. However, the NIRS optode coverage is on a two dimensional manifold and the representation over the fMRI map has to be two dimensional. Hence, the two dimensional interpolation function is sufficient to represent the interpolated NIRS signals. Therefore, the resultant random field is assumed two dimensional.

References

- Adler, R.J., 1981. The Geometry of Random Fields. John Wiley & Sons, New York.
- Adler, R.J., 2000. On excursion sets, tube formulae, and maxima of random fields. Ann. Appl. Probab. 10 (1), 1–74.
- Adler, R., Taylor, J., 2007. Random Fields and Geometry. Springer, New York.
- Beckmann, C., Jenkinson, M., Smith, S., 2003. General multilevel linear modeling for group analysis in fMRI. NeuroImage 20 (2), 1052–1063.
- Benaron, D., Hintz, S., Villringer, A., Boas, D., Kleinschmidt, A., Frahm, J., Hirth, C., Obrig, H., van Houten, J., Kermit, E., et al., 2000. Noninvasive functional imaging of human brain using light. J. Cereb. Blood Flow Metab. 20, 469–477.
- Boas, D.A., O'Leary, M.A., Chance, B., Yodh, A.G., July 1997. Detection and characterization of optical inhomogeneities with diffuse photon density waves: a signal-to-noise analysis. Appl. Opt. 36, 75–92.
- Boas, D., Brooks, D., Miller, E., DiMarzio, C., Kilmer, M., Gaudette, R., 2001. Imaging the body with diffuse optical tomography. IEEE Signal Process. Mag. 18 (6), 57–75.
- Boas, D., Strangman, G., Culver, J., Hoge, R., Jasdzewski, G., Poldrack, R., Rosen, B., Mandeville, J., 2003. Can the cerebral metabolic rate of oxygen be estimated with near-infrared spectroscopy? Phys. Med. Biol. 48 (15), 2405–2418.
- Boas, D., Dale, A., Franceschini, M., 2004. Diffuse optical imaging of brain activation: approaches to optimizing image sensitivity, resolution, and accuracy. NeuroImage 23, 275–288.
- Bullmore, E., Brammer, M., Williams, S.C., Rabe-Hesketh, S., Janot, N., David, A., Mellers, J., Howard, R., Sham, P., 1996. Statistical methods of estimation and inference for functional MR image analysis. Magn. Reson. Med. 35, 261–277.
- Cannestra, A., Pouratian, N., Bookheimer, S., Martin, N., Becker, D., Toga, A., 2001. Temporal spatial differences observed by functional MRI and human intraoperative optical imaging. Cereb. Cortex 11 (8), 773–782.
- Cao, J., Worsley, K., 1999a. The detection of local shape changes via the geometry of Hotelling's T^2 fields. Ann. Stat. 27 (3), 925–942.
- Cao, J., Worsley, K., 1999b. The geometry of the Hotelling's random field with applications to the detection of shape changes. Ann. Stat. 27 (3), 925–942.
- Chen, Y., Tailor, D., Intes, X., Chance, B., 2003. Correlation between near-infrared spectroscopy and magnetic resonance imaging of rat brain oxygenation modulation. Phys. Med. Biol. 48 (4), 417–427.
- Cope, M., Delpy, D.T., May 1988. System for long-term measurement of cerebral blood and tissue oxygenation on newborn infants by near infra-red transillumination. Med. Biol. Eng. Comput. 26, 289–294.
- Friston, K.J., Holmes, A.P., Poline, J.B., Price, C.J., Frith, C.D., December 1996. Detecting activations in PET and fMRI: levels of inference and power. NeuroImage 40, 223–235.

- Friston, K.J., Josephs, O., Zarahn, E., Holmes, A.P., Rouquette, S., Poline, J.B., August 2000. To smooth or not to smooth? Bias and efficiency in fMRI time-series analysis. *NeuroImage* 12, 196–208.
- Friston, K.J., Penny, W.D., Phillips, C., Kiebel, S., Hinton, G., Ashburner, J., June 2002. Classical and Bayesian inference in neuroimaging: theory. *NeuroImage* 16, 465–483.
- Friston, K.J., Ashburner, J., Kiebel, S., Nichols, T., Penny, W. (Eds.), 2006. Statistical Parametric Mapping: The Analysis of Functional Brain Images. Academic Press, San Diego, CA, USA.
- Fujiwara, N., Sakatani, K., Katayama, Y., Murata, Y., Hoshino, T., Fukaya, C., Yamamoto, T., 2004. Evoked-cerebral blood oxygenation changes in false-negative activations in BOLD contrast functional MRI of patients with brain tumors. *NeuroImage* 21 (4), 1464–1471.
- Hess, A., Stiller, D., Kaulisch, T., Heil, P., Scheich, H., 2000. New insights into the hemodynamic blood oxygenation level-dependent response through combination of functional magnetic resonance imaging and optical recording in gerbil barrel cortex. *J. Neurosci.* 20 (9), 3328–3338.
- Hofmann, M.J., Herrmann, M.J., Dan, I., Obrig, H., Conrad, M., Kuchinke, L., Jacobs, A.M., Fallgatter, A.J., 2008. Differential activation of frontal and parietal regions during visual word recognition: an optical topography study. *NeuroImage* 40 (3), 1340–1349.
- Hoge, R., Franceschini, M., Covolan, R., Huppert, T., Mandeville, J., Boas, D., 2005. Simultaneous recording of task-induced changes in blood oxygenation, volume, and flow using diffuse optical imaging and arterial spin-labeling MRI. *NeuroImage* 25 (3), 701–707.
- Homan, R.W., Herman, J., Purdy, P., April 1987. Cerebral location of international 10–20 system electrode placement. *Electroencephalogr. Clin. Neurophysiol.* 66, 376–382.
- Horn, B.K.P., April 1987. Closed-form solution of absolute orientation using unit quaternions. *J. Opt. Soc. Amer. A* 4, 629–642.
- Hoshi, Y., 2007. Functional near-infrared spectroscopy: current status and future prospects. *J. Biomed. Opt.* 12, 062106.
- Hoshi, Y., Tsou, B., Billock, V., Tanosaki, M., Iguchi, Y., Shimada, M., Shinba, T., Yamada, Y., Oda, I., 2003. Spatiotemporal characteristics of hemodynamic changes in the human lateral prefrontal cortex during working memory tasks. *NeuroImage* 20 (3), 1493–1504.
- Huppert, T., Hoge, R., Diamond, S., Franceschini, M., Boas, D., 2006. A temporal comparison of BOLD, ASL, and NIRS hemodynamic responses to motor stimuli in adult humans. *NeuroImage* 29 (2), 368–382.
- Jain, A.K., 1989. Fundamentals of Digital Image Processing. Prentice Hall, Englewood Cliffs, New Jersey.
- Jobson, F.F., December 1977. Noninvasive, infrared monitoring of cerebral and myocardial oxygen sufficiency and circulatory parameters. *Science* 198, 1264–1267.
- Johansen, S., Johnstone, I., 1990. Hotelling's theorem on the volume of tubes: some illustrations in simultaneous inference and data analysis. *Ann. Stat.* 18 (2), 652–684.
- Klein Schmidt, A., Obrig, H., Requardt, M., Merboldt, K., Dirnagl, U., Villringer, A., Frahm, J., 1996. Simultaneous recording of cerebral blood oxygenation changes during human brain activation by magnetic resonance imaging and near-infrared spectroscopy. *J. Cereb. Blood Flow Metab.* 16, 817–826.
- Koh, P.H., Glaser, D.E., Flandin, G., Kiebel, S., Butterworth, B., Maki, A., Delpy, D.T., Elwell, C.E., November 2007. Functional optical signal analysis: a software tool for near-infrared spectroscopy data processing incorporating statistical parametric mapping. *J. Biomed. Opt.* 12, 1–13.
- Korn, G.A., Korn, T.M. (Eds.), 1968. Mathematical Handbook for Scientists and Engineers. McGraw Hill, New York.
- Logothetis, N., 2003. The underpinnings of the BOLD functional magnetic resonance imaging signal. *J. Neurosci.* 23 (10), 3963.
- MacIntosh, B., Klassen, L., Menon, R., 2003. Transient hemodynamics during a breath hold challenge in a two part functional imaging study with simultaneous near-infrared spectroscopy in adult humans. *NeuroImage* 20 (2), 1246–1252.
- Mandeville, J., Marota, J., Ayata, C., Moskowitz, M., Weisskoff, R., Rosen, B., 1999. MRI measurement of the temporal evolution of relative CMRO₂ during rat forepaw stimulation. *Magn. Reson. Med.* 42 (5), 944–951.
- Mehagnoul-Schipper, D., van der Kallen, B., Colier, W., van der Sluijs, M., van Erning, L., Thijssen, H., Oeseburg, B., Hoefnagels, W., Jansen, R., 2002. Simultaneous measurements of cerebral oxygenation changes during brain activation by near-infrared spectroscopy and functional magnetic resonance imaging in healthy young and elderly subjects. *Hum. Brain Mapp.* 16 (1), 14–23.
- Murata, Y., Sakatani, K., Katayama, Y., Fukaya, C., 2002. Increase in focal concentration of deoxyhaemoglobin during neuronal activity in cerebral ischaemic patients. *Br. Med. J.* 323 (2), 182.
- Obrig, H., Villringer, A., 2003. Beyond the visible? Imaging the human brain with light. *J. Cereb. Blood Flow Metab.* 23, 1–18.
- Okamoto, M., Dan, H., Sakamoto, K., Takeo, K., Shimizu, K., Kohno, S., Oda, I., 2004a. Three-dimensional probabilistic anatomical crano-cerebral correlation via the international 10–20 system oriented for transcranial functional brain mapping. *NeuroImage* 21, 99–111.
- Okamoto, M., Dan, H., Shimizu, K., Takeo, K., Amita, T., Oda, I., Konishi, I., Sakamoto, K., Isobe, S., Suzuki, T., et al., 2004b. Multimodal assessment of cortical activation during apple peeling by NIRS and fMRI. *NeuroImage* 21 (4), 1275–1288.
- Okamoto, M., Matsunami, M., Dan, H., Kohata, T., Kohyama, K., Dan, I., et al., 2006. Prefrontal activity during taste encoding: an fNIRS study. *NeuroImage* 31 (2), 796–806.
- O'Leary, M., Boas, D., Chance, B., Yodh, A., 1995. Experimental images of heterogeneous turbid media by frequency-domain diffusing-photon tomography. *Opt. Lett.* 20 (5), 426–428.
- Plichta, M., Herrmann, M., Baehne, C., Ehli, A., Richter, M., Pauli, P., Fallgatter, A., 2006. Event-related functional near-infrared spectroscopy (fNIRS): are the measurements reliable? *NeuroImage* 31 (1), 116–124.
- Plichta, M.M., Heinzel, S., Ehli, A.C., Pauli, P., Fallgatter, A.J., April 2007. Model-based analysis of rapid event-related functional near-infrared spectroscopy (NIRS) data: a parametric validation study. *NeuroImage* 35, 625–634.
- Schroeter, M.L., Bucheler, M.M., Müller, K., Uludag, K., Obrig, H., Lohmann, G., Tittgemeyer, M., Villringer, A., von Cramon, D.Y., January 2004. Towards a standard analysis for functional near-infrared imaging. *NeuroImage* 21, 283–290.
- Siegel, A., Culver, J., Mandeville, J., Boas, D., 2003. Temporal comparison of functional brain imaging with diffuse optical tomography and fMRI during rat forepaw stimulation. *Phys. Med. Biol.* 48 (10), 1391–1403.
- Smith, E.E., Jonides, J., Marshuetz, C., Koeppe, R.A., 1998. Components of verbal working memory: evidence from neuroimaging. *Proc. Natl. Acad. Sci.* 95, pp. 876–882.
- Steinbrink, J., Villringer, A., Kempf, F., Haux, D., Boden, S., Obrig, H., 2006. Illuminating the BOLD signal: combined fMRI-NIRS studies. *Magn. Reson. Imaging* 24 (4), 495–505.
- Strangman, G., Culver, J., Thompson, J., Boas, D., 2002. A quantitative comparison of simultaneous BOLD fMRI and NIRS recordings during functional brain activation. *NeuroImage* 17 (2), 719–731.
- Sun, J., January 1993. Tail probabilities of the maxima of Gaussian random fields. *Ann. Probab.* 21 (1), 34–71.
- Sun, J., Loader, C., 1994. Simultaneous confidence bands for linear regression and smoothing. *Ann. Stat.* 22 (3), 1328–1345.
- Takemura, A., Kuriki, S., 2002. On the equivalence of the tube and Euler characteristic methods for the distribution of the maximum of Gaussian fields over piecewise smooth domains. *Ann. Appl. Probab.* 12 (2), 768–796.
- Taylor, J., Adler, R., 2003. Euler characteristics for Gaussian fields on manifolds. *Ann. Probab.* 31 (2), 533–563.
- Taylor, J., Worsley, K., 2007. Detecting sparse signals in random fields, with an application to brain mapping. *J. Am. Stat. Assoc.* 102 (479), 913–928.
- Taylor, J., Worsley, K., 2008. Random fields of multivariate test statistics, with application to shape analysis. *Ann. Stat.* 36 (1), 1–27.
- Torontov, V., Webb, A., Choi, J., Wolf, M., Michalos, A., Gratton, E., Hueber, D., 2001. Investigation of human brain hemodynamics by simultaneous near-infrared spectroscopy and functional magnetic resonance imaging. *Med. Phys.* 28, 521.
- Torontov, V., Walker, S., Gupta, R., Choi, J., Gratton, E., Hueber, D., Webb, A., 2003. The roles of changes in deoxyhemoglobin concentration and regional cerebral blood volume in the fMRI BOLD signal. *NeuroImage* 19 (4), 1521–1531.
- Tsujimoto, S., Yamamoto, T., Kawaguchi, H., Koizumi, H., Sawaguchi, T., 2004. Prefrontal cortical activation associated with working memory in adults and preschool children: an event-related optical topography study. *Cereb. Cortex* 14 (7), 703–712.
- Tsuzuki, D., Jurcak, V., Singh, A., Okamoto, M., Watanabe, E., Dan, I., 2007. Virtual spatial registration of stand-alone fNIRS data to MNI space. *NeuroImage* 34 (4), 1506–1518.
- Villringer, A., Dirnagl, U., 1995. Coupling of brain activity and cerebral blood flow: basis of functional neuroimaging. *Cerebrovasc. Brain Metab. Rev.* 7, 240–276.
- Wei, X., Yoo, S.S., Dickey, C.C., Zou, K.H., Guttman, C.R.G., Panych, L.P., March 2004. Functional MRI of auditory verbal working memory: long-term reproducibility analysis. *NeuroImage* 21, 1000–1008.
- Weyl, H., 1939. On the volume of tubes. *Amer. J. Math* 61 (2), 461–472.
- Worsley, K.J., 1994. Local maxima and the expected Euler characteristic of excursion sets of χ^2 , F and t fields. *Advances in Applied Probability* 1 (26), 13–42.
- Worsley, K.J., 1995. Boundary corrections for the expected Euler characteristic of excursion sets of random fields, with an application to astrophysics. *Adv. Appl. Probab.* 4 (27), 943–959.
- Worsley, K.J., Friston, K.J., 1995. Analysis of fMRI time-series revisited-again. *NeuroImage* 2, 173–181.
- Worsley, K., Andermann, M., Kouli, T., MacDonald, D., Evans, A., 1999. Detecting changes in nonisotropic images. *Hum. Brain Mapp.* 8, 98–101.
- Yamamoto, T., Kato, T., 2002. Paradoxical correlation between signal in functional magnetic resonance imaging and deoxygenated haemoglobin content in capillaries: a new theoretical explanation. *Phys. Med. Biol.* 47 (7), 1121–1141.
- Ye, J.C., Moulin, P., Bresler, Y., October 2006. Asymptotic global confidence regions for 3-D parametric shape estimation in inverse problems. *IEEE Trans. Image Process.* 15 (10), 2904–2919.
- Zhao, H., Tanikawa, Y., Gao, F., Onodera, Y., Sassaroli, A., Tanaka, K., Yamada, Y., 2002. Maps of optical differential path length factor of human adult forehead, somatosensory motor and occipital regions at multi-wavelengths in NIR. *Phys. Med. Biol.* 47 (12), 2075–2093.